Theoretical Diagnostic Analysis of K_α Emission Spectra Obtained in PBFA-II Lithium Beam Experiments

J.J. MacFarlane and P. Wang

March 1994

UWFDM-945

FUSION TECHNOLOGY INSTITUTE

UNIVERSITY OF WISCONSIN

MADISON WISCONSIN

Theoretical Diagnostic Analysis of K_α Emission Spectra Obtained in PBFA-II Lithium Beam Experiments

J.J. MacFarlane and P. Wang

Fusion Technology Institute
University of Wisconsin
1500 Engineering Drive
Madison, WI 53706

http://fti.neep.wisc.edu

March 1994

UWFDM-945

Theoretical Diagnostic Analysis of K_α Emission Spectra Obtained in PBFA-II Lithium Beam Experiments

J. J. MacFarlane and P. Wang

Fusion Technology Institute
University of Wisconsin
Madison, WI 53719

March 1994

UWFDM-945

Table of Contents

Section 1

Introduction

The purpose of this report is to summarize work performed for Sandia National Laboratories during the period March 1993-March 1994. The primary objective of this work is to provide theoretical support for the analyses of spectral measurements obtained in Particle Beam Fusion Accelerator-II (PBFA-II) experiments. In our analyses, we use: (1) a collisional-radiative equilibrium (CRE) code in which multilevel statistical equilibrium equations are solved self-consistently with the radiation field and ion beam properties; and (2) a suite of atomic physics codes which provide high quality atomic structure and cross section data for the many radiative and collisional processes that can occur in light ion beam-plasma interaction experiments. The major features of the CRE and atomic physics codes are listed in Tables 1.1 and 1.2, respectively.

The statement of work for the past year is shown in Table 1.3. The primary objective of this year was to analyze x-ray spectra obtained in PBFA-II lithium beam experiments. These spectra were obtained in experiments using planar, "plastic sandwich" targets (CH : Al : Au : CH). Our efforts this year included the following. First, we have improved our atomic models to provide more accurate calculated wavelengths for the K_α transitions of moderate-Z elements (such as Al). As a check, we compared our new wavelengths and oscillator strengths for Al with calculations from Chen and Iglesias (1993) and the published data of Boiko et al. (1978). Also, a more detailed atomic model is used as we now consider fine-structure splitting in our calculations. The new atomic model calculations are described in Section 2.A. In Section 2.B, we compare results of our models with a measured Al K_α absorption spectrum obtained in a LLNL laser-produced plasma experiment (Perry et al. 1991) and a PBFA-II K_α emission spectrum. Experimental K_α absorption spectra provide very valuable tests for our models for two reasons. First, the spectral resolution in the LLNL experiments was about $\lambda/\Delta\lambda \approx 2500$, which is about a factor of 2 higher than that used in previous PBFA-II experiments (Bailey et al. 1990; 1993). Second, absorption spectra provide a measure of the population of the *lower* state of each transition, as opposed the upper state in emission measurements. Thus, the analysis of absorption spectra is not complicated by uncertainties in Li beam-impact ionization cross sections, which are required to predict the populations of autoionizing levels (i.e., the upper states in PBFA-II emission spectra).

Table 1.1. Major Features of Collisional-Radiative Equilibrium Code

- Multilevel, steady-state atomic rate equations are solved self-consistently with the radiation field and ion beam properties.
- Any state in the atomic model can be coupled to any other state; thus, transitions between excited states of differing ions can be considered, as can transitions between non-adjacent ions.
- Ion beam-induced multiple ionization effects are included as direct transitions in the statistical equilibrium matrix equations.
- Emission and absorption spectra include contributions from bound-bound (lines), bound-free (recombinations), and free-free transitions (Bremsstrahlung).
- Inner-shell line emission induced by intense ion beams is calculated by tracking the populating and depopulating rates of autoionizing levels which are explicitly included in the model.
- Line shapes include effects of natural, Doppler, Auger, and Stark broadening.
- Radiation transport is modeled using either:

  (i) an angle- and frequency-averaged escape probability method, or

  (ii) a multiangle, multifrequency model based on the second-order form of the transfer equation.

Table 1.2. Major Features of Atomic Physics Models

- Atomic structure and radiative data are computed using configuration interaction (CI) method with Hartree-Fock wavefunctions.
- Multiconfiguration Hartree-Fock and Dirac-Fock calculations provide accurate transition energies and oscillator strengths for lines of interest.
- Atomic collisional data are computed using a combination of distorted wave, Coulomb-Born, and semiclassical impact parameter models.
- Ion-impact ionization cross sections are computed using a plane-wave Born approximation model with Hartree-Fock wavefunctions and with the inclusion of binding energy, Coulomb-deflection, and relativistic corrections.
- Multiple ionization cross sections are computed using an independent event model with a binomial distribution probability.
- Term-dependent Auger rates and fluorescence yields are calculated using an LS coupling formalism with Hartree-Fock wavefunctions.

Table 1.3. Tasks for March 1993 – March 1994

1. Generate atomic models for target materials and compute relevant beam-plasma interaction cross sections for predicting inner-shell line emission.
2. Analyze spectral data obtained in PBFA-II experiments. Perform CRE calculations to determine plasma conditions obtained in experiments.
3. Document results in a final report to Sandia National Laboratories.
4. Update source code for the CRE/transport package on Sandia's computer system as necessary.

Several series of CRE calculations were performed for plasmas of uniform temperature and density to study the dependence of Al K_α emission and absorption spectra on plasma conditions. Section 2.C shows computed spectra for a range of plasma conditions relevant to recent PBFA-II experiments. The absorption spectra also show the presence of K_β lines ($1s \rightarrow 3p$ transitions) which also could be used as a diagnostic if an x-ray backlighter could be utilized in experiments. In Section 2.D, we describe how the intensity ratios of K_α emission lines can be used to constrain plasma temperatures and densities. We believe that this technique could be very valuable in diagnosing plasma conditions in PBFA-II target experiments. This analysis is applied to PBFA-II spectra obtained in early 1993, where it is shown that a consistent temperature and density range is predicted from several pairs of lines. Although the densities found are roughly consistent with those obtained from radiation-hydrodynamics simulations of the experiment (Dukart 1993), the temperatures are about 60% higher (44 eV vs. 27 eV) than the radiation-hydrodynamics results. One possible reason for this discrepancy is that the radiation-hydrodynamic simulations could be overestimating radiation losses in the Al layer. This is discussed in Section 2.F.

We have also investigated the influence of dielectronic recombination on K_α emission spectra in PBFA-II experiments. This work is described in Section 2.E. Here, it is found that dielectronic recombination likely has little effect on K_α spectra measured in PBFA-II experiments to date because plasma temperatures have been $\lesssim 50$ eV. However, when plasma temperatures reach $\gtrsim 70-100$ eV it is predicted that the role of dielectronic recombination can be important because the rate at which it populates autoionizing levels becomes comparable to that of ion beam-impact ionization.

Sections 3 and 4 contain papers recently presented at the 6th International Workshop on Atomic Physics for Ion-Driven Fusion, which took place in Santa Fe, NM in November 1993. Section 3 summarizes some of our work in calculating K_α emission and absorption spectra. Section 4 presents a discussion of our model for computing multiple ionization cross sections. Multiple ionization — that is, the simultaneous ejection of more than one electron from a target ion caused by its interaction with a fast (beam) ion — plays an important role in the formation of K_α emission spectra in Li beam experiments.

Finally, we wish to acknowledge the many valuable discussions we have had with Sandia personnel; in particular, Jim Bailey, Tom Mehlhorn, and Ray Dukart. Much of this work is based on their suggestions and insights. In addition, this work has benefitted substantially from our collaboration with the KALIF program at Kernforschungszentrum Karlsruhe (KfK). Much of the development of our CRE and atomic physics codes has been supported by KfK.

Section 2

Analysis of Aluminum K_α Spectra Obtained in PBFA-II Li Beam Experiments

We have made substantial progress in our ability to diagnose plasma conditions in PBFA-II experiments using K_α emission spectroscopy. In previous work (MacFarlane and Wang 1993) synthetic time-dependent and time-integrated spectra for Al were computed utilizing temperature and density distributions obtained from 1-D LASNEX calculations (Dukart 1993). The calculated time-integrated spectra were then compared with measured emission spectra obtained using an x-ray elliptic crystal spectrograph (Bailey 1993). From this analysis, a peak temperature of between 39 and 47 eV for PBFA-II Shot 5881 was estimated based on the "gross" features of the K_α emission spectrum; i.e., the relative strengths of major spectral features (corresponding to ions ranging from neutral through He-like Al). Recall that the targets in this experimental series were planar "plastic sandwich" targets with thin layers of Al and Au sandwiched between CH tampers (see Fig. 2 of Section 3).

During the past year, we have investigated whether measured intensity ratios of K_α emission lines could be used to accurately determine target plasma conditions. Line intensity ratio analyses have been used extensively to determine temperatures and densities for both laboratory and astrophysical plasmas. However, the situation is somewhat unique in PBFA-II experiments in that the emission lines are produced by non-thermal effects (i.e., the ion beam). Below, we describe how this method can be used to ascertain target plasma conditions in PBFA-II experiments, and apply this method to PBFA-II Shot 5881. This work is discussed in Section 2.D.

Efforts were made in several additional areas to improve our theoretical capabilities and assist in the interpretation of the K_α diagnostic experiments. First, we have improved our atomic model for moderate-Z elements (e.g., Al). We now include fine-structure splitting of all levels involved in K_α transitions (as opposed to using an L-S term split model in previous work). Also, a modified method for estimating electron correlation effects was used. This produced better agreement with experimental and calculated K_α wavelengths. This work is discussed in Sections 2.A and 2.B. Second, we have examined the effects of dielectronic recombination on Al emission spectra obtained in PBFA-II experiments. Our results, discussed in Section 2.E, predict that at temperatures achieved to date in PBFA-II experiments (up to roughly 40-50 eV) the contribution of dielectronic

recombination to the K_α spectrum is negligible, but becomes more important at higher plasma temperatures.

Finally, to assist in the interpretation of radiation-hydrodynamics calculations, we have computed the radiative properties of a thin Al plasma using our detailed radiation transport and atomic models, and compared them to the flux predicted in a 1-D LASNEX calculation. Our results suggest that the radiation model in LASNEX *may* be significantly overestimating the radiation energy loss rate in the Al layer of the plastic sandwich target. If so, peak temperatures predicted by LASNEX would be underestimated. This explanation may account for the "inconsistency" between the measured beam intensity and the peak temperature inferred from the K_α spectrum. These calculations are described in Section 2.F.

2.A. Improvements to Atomic Structure Modeling

In this section, we describe improvements we have made in our atomic structure calculations. These improvements lead to better agreement between calculated wavelengths and experimental data than previously achieved. In particular, we have improved our method for computing the wavelengths of K_α lines, and we now consider fine-structure splitting for all energy levels involved in K_α transitions.

In our previous analyses of aluminum K_α spectra measured in PBFA-II experiments, an LS term structure model was used. LS term structure modeling is believed to be sufficient for line identification in K_α spectral measurements. As an example, Figs. 2.1 through 2.3 show calculated stick spectra (oscillator strength vs. photon energy) for Li-, Be-, and B-like Al K_α transitions. In each case, the LS term spectra (top) are compared with calculated fine-structure spectra (bottom). Also shown in the figures (as dashed curves) is the experimental data of Perry et al. (1991). It can be seen from the figures that each major peak of the experimental data corresponds well to a strong LS term-dependent line. Typical fine-structure splittings are $\lesssim 2-3$ mÅ. Fine structure splittings tend not to be individually resolved in the Perry data because of the limitaton of detector resolution ($\Delta\lambda \approx 3$ mÅ). However, fine-structure splitting could affect the broadening of the features in the experimental data. In recent PBFA-II experiments, the resolution of the elliptic crystal spectrograph used to observe K_α spectra was about $\lambda/\Delta\lambda \sim 1200$. Thus, fine-structure splitting could not be resolved. However, the fine-structure splitting can be comparable to the intrinsic (Auger broadened) lines widths ($\sim$ a mÅ or so). In this case, both emission and absorption spectra can potentially

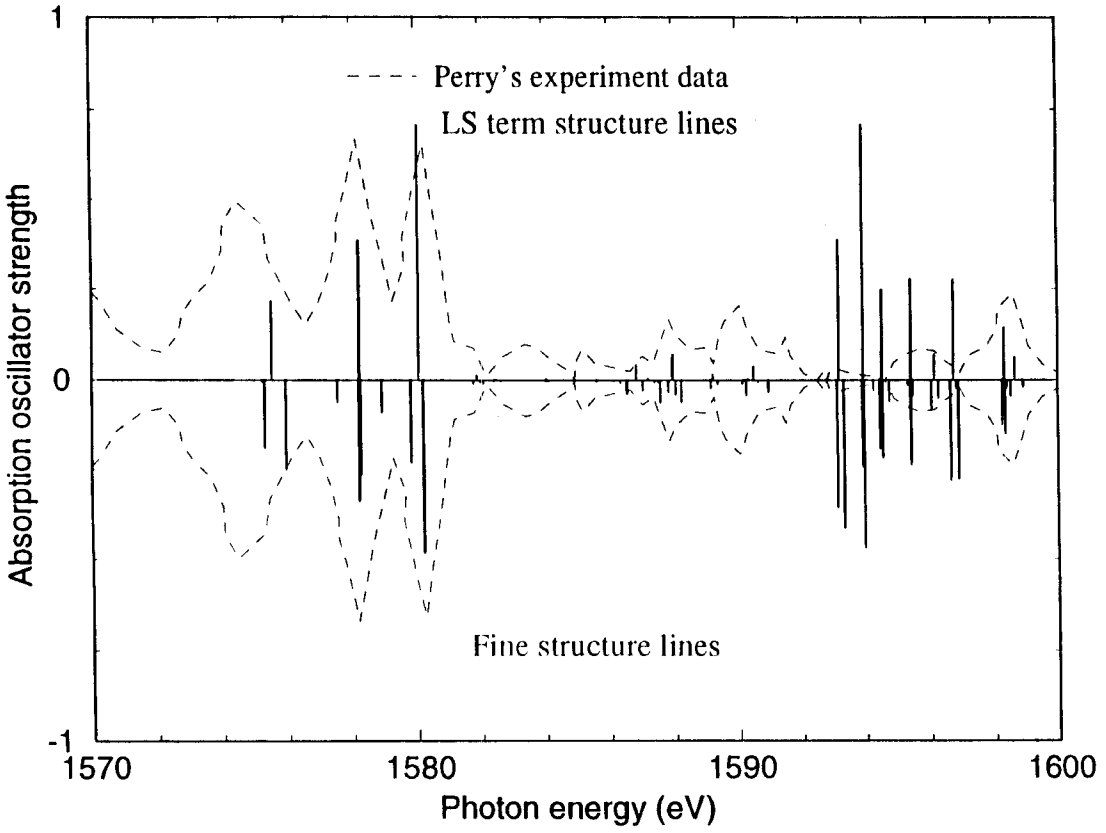

Figure 2.1. Comparison of K_α "stick spectra" for Li-like Al computed using atomic models with L-S term splitting (upper half of plot) and fine-structure splitting. Also shown (as dashed curves) is the experimental absorption spectrum of Perry et al. (1991).

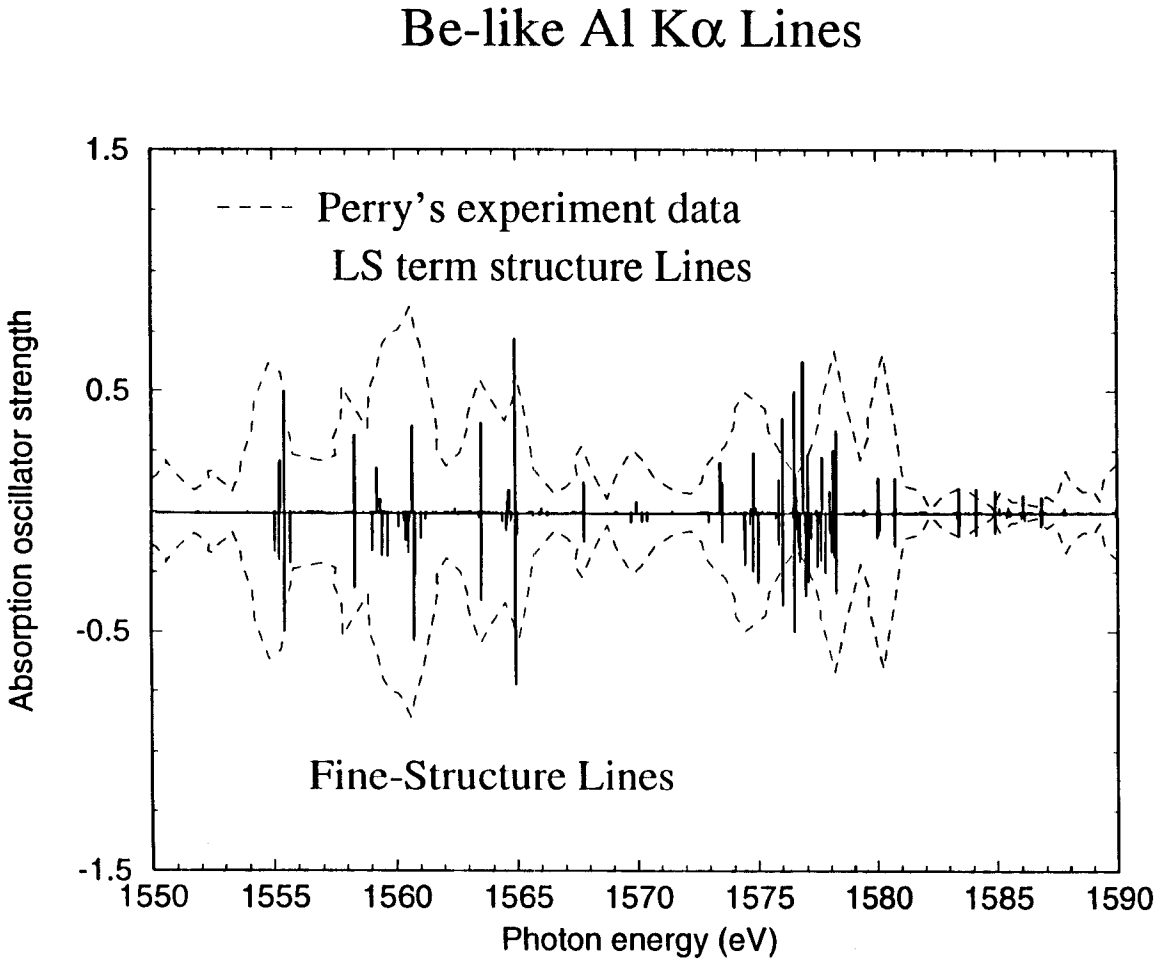

Figure 2.2. Comparison of K_α "stick spectra" for Be-like Al computed using atomic models with L-S term splitting (upper half of plot) and fine-structure splitting. Also shown (as dashed curves) is the experimental absorption spectrum of Perry et al. (1991).

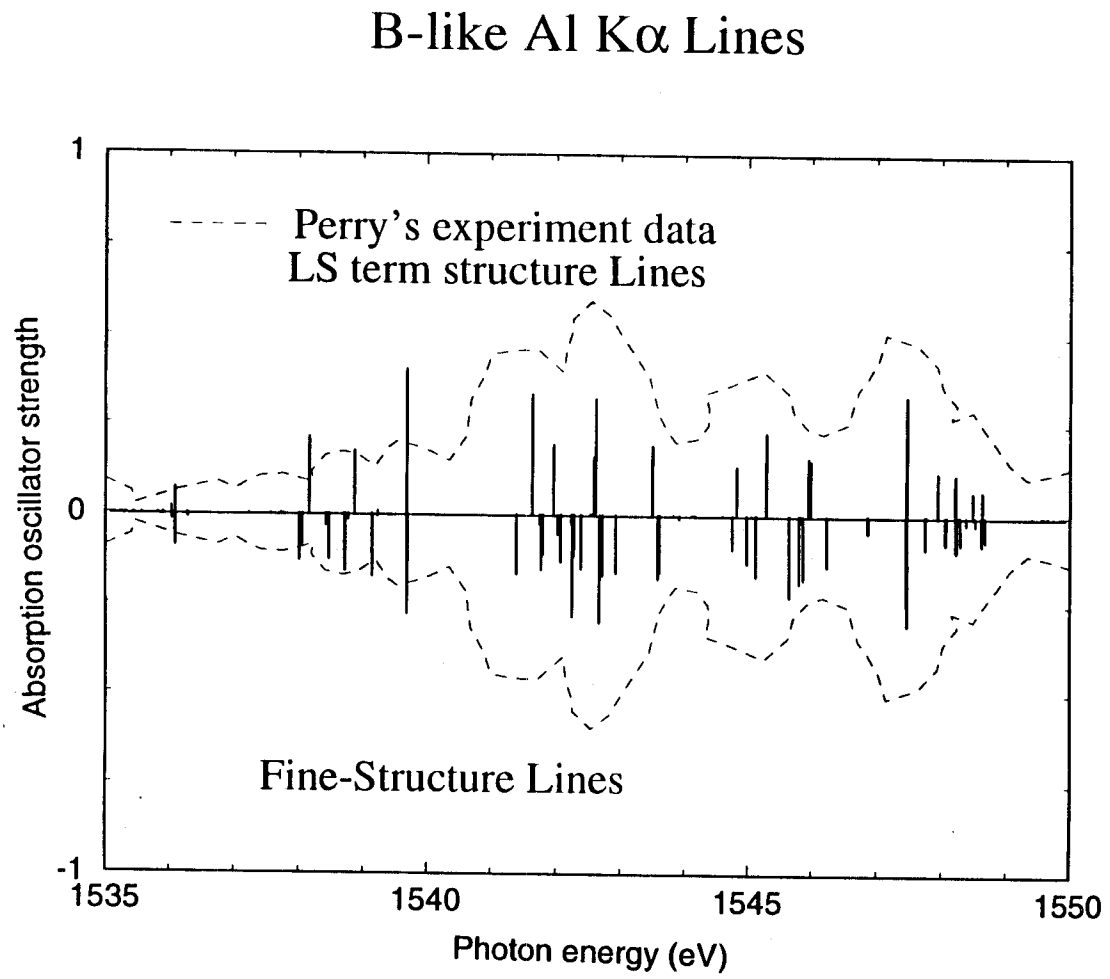

Figure 2.3. Comparison of K_α "stick spectra" for B-like Al computed using atomic models with L-S term splitting (upper half of plot) and fine-structure splitting. Also shown (as dashed curves) is the experimental absorption spectrum of Perry et al. (1991).

be affected (emission because of resonant self-absorption effects, and absorption because of saturation effects). Because of this, we now include in our new atomic model fine-structure splitting for all levels involved in K_α transitions.

Figure 2.1 also shows the presence of several Li-like lines near the He_α line at 1.593 to 1.598 keV. These are K_α transitions with M-shell spectators ($1s^1 2p^1 3l^1 \rightarrow 1s^2 3l^1$), and could potentially produce emission on the long wavelength side of the He_α line. At present, our calculations suggest the emission should be too weak to be observed. Additional calculations are being performed to analyze this in more detail.

We summarize our new atomic model as follows:

- Full intermediate coupling (fine-structure) for all levels of electronic configurations with $n \leq 3$ and $l \leq 2$. This basically covers all K_α transitions which make contributions to the satellite spectrum.
- Pure LS coupling (LS term structure) for levels of electronic configurations with $4 \leq n \leq 6$ and $l \leq 3$.
- Configuration average and complex structure for all levels of electronic configurations with $n \geq 7$ and $l \geq 3$.

It has long been a problem for first principles self-consistent-field (SCF) atomic structure calculations to produce highly accurate wavelengths consistently for large scale atomic models. This is particularly true for configuration interaction (CI) calculations because the characteristics of the CI expansion can be very different for different atomic states. Very accurate wavelengths and oscillator strengths can be obtained for a specific transition if both correlation and relativistic effects are carefully accounted for in the CI calculation. For large scale calculations, however, the configurations used in the CI expansions for each ion are limited. The accuracy of wavelengths for different lines can be different even when they are produced in the same calculation. This is because the same CI expansion may be sufficiently complete for some atomic states but not for others. This is why in our previous calculations some K_α wavelengths agreed very well with the experimental data while others were not as accurate.

Both correlation and relativistic effects are crucial for the calculation of K_α transition energies (Wang et al. 1993). Generally speaking, correlation and relativistic effects cause opposing shifts in the K_α transition energies and cancel each other to some degree. If one neglects relativistic corrections in a calculation, the resulting wavelengths

of K_α transitions will have a redshift. On the other hand, if one takes full account of relativistic effects while only partially accounting for correlation effects, the resulting wavelengths will have a blueshift. In our previous atomic structure calculations, the relativistic effects were taken into account using Breit-Pauli relativistic corrections, and correlation effects were included using configuration interaction expansions. Depending on the selection of configurations used in the CI expansions, the wavelengths of some K_α lines may vary by a few mÅ. This is because a large number of configurations is required in the CI expansions to fully account for the correlation effects. One simple way to solve this problem is to include as many configurations as possible into the CI expansions. However, this is not practical in large scale calculations. Therefore, we have developed a "relativistic scale factor method" to deal with this problem.

First, we note that correlation effects are usually underestimated for a limited CI expansion. Because correlation effects and relativistic effects cause opposing shifts in the K_α transition energies, the relativistic correction terms can be scaled down proportionally so that the net corrections to the K_α transition energies are the same as those from calculations which more fully account for both relativistic and correlation effects. The relativistic term is adjusted (instead of the correlation term) because it is computed explicitly. Stated mathematically:

$$\Delta E_{\mathrm{partial-correlation}} + \Delta E_{\mathrm{partial-relativistic}} = \Delta E_{\mathrm{full-correlation}} + \Delta E_{\mathrm{full-relativistic}} \,.$$

In this way, if the scaling factor is chosen properly one can obtain very good results with a relatively small number of configurations in the CI expansions. We have used this "scaling factor method" in our new atomic structure calculations. We note, however, that while this approach works well for inner-shell transitions, it would not be particularly accurate for valence shell transitions where correlation effects dominate.

Clearly, the most crucial part in using this approach is the determination of scaling factors. In our calculations we have used a semi-empirical method for determining the scaling factors for each ion. First, we perform detailed calculations for a few K_α lines for each ion with a large number of configurations in the CI expansion. The results of these refined calculations should be quite accurate. Then we set up CI expansion bases for large scale calculations. For each ion, we adjust the relativistic correction factor in the large scale calculation to fit the wavelengths to those of the detailed calculations. In Table 2.1 we list the scaling factors used in our large scale calculations for aluminum ions. It should be noted that the scaling factor increases with increasing ionization stage. This occurs because correlation effects are greater for ions with more bound electrons.

Table 2.1. Relativistic Scaling Factors for Al Ions

Ion	Scaling Factor	Number of Configurations in CI Expansion
Al I	0.75	15
Al II	0.78	15
Al III	0.78	14
Al IV	0.80	14
Al V	0.80	14
Al VI	0.83	13
Al VII	0.85	13
Al VIII	0.90	13
Al IX	0.92	13
Al X	0.96	13
Al XI	1.00	10

Some results from our new calculations are listed in Tables 2.2 through 2.4. Table 2.2 shows K_α transition data for the strongest He-like and Li-like satellites. Also shown are experimental wavelengths listed in Boiko et al. (1978). It is seen that our results agree very well with the experimental data. The strongest lines for the Be-like satellites are given in Table 2.3 and compared with M. Chen's multiconfiguration Dirac-Fock calculations (Chen and Iglesias 1993). The agreement between the two sets of calculations is very good. Differences in wavelengths are typically a few mÅ. It should be mentioned that Chen's calculation was a full relativistic multiconfiguration calculation, while our calculation is a semi-relativistic configuration interaction calculation. The good agreement between two sets of calculation shows that our treatment of scaling relativistic correction to compensate for correlation effects is reasonable. Table 2.4 shows the transitions for the strongest B-like satellites. We expect that the accuracy of the calculated wavelengths is similar to those of the Li-like and Be-like lines.

2.B. Al K_α Line ID: Comparison of Calculated Spectra With Measured K_α Absorption and Emission Spectra

Using the new atomic model described in the previous section, we now compare computed spectra with two types of measured Al spectra: K_α emission spectra obtained in PBFA-II Li beam experiments, and K_α absorption spectra obtained in LLNL laser-produced plasma experiments. In the laser-plasma experiments a high-Z material is

Table 2.2. Strongest He- and Li-like K_α Transitions for Aluminum

		This calculation		Exp. Data	
Lower Level	Upper Level	Wavelength (Å)	f-value	Wavelength (Å)	Identification
$1s^2$ $^1S)$ $^1S_{0.0}$	$1s^1\ 2p^1$ $^2S)$ $^3P_{1.0}$	7.805	1.63E-03	7.805	He[IC]
$1s^2$ $^1S)$ $^1S_{0.0}$	$1s^1\ 2p^1$ $^2S)$ $1P_{1.0}$	7.756	8.01E-01	7.757	He_α
$1s^2\ 2p^1$ $^1S)$ $^2P_{0.5}$	$1s^1\ 2p^2$ $^2S)$ $^2S_{0.5}$	7.795	3.13E-02	7.796	n
$1s^2\ 2p^1$ $^1S)$ $^2P_{1.5}$	$1s^1\ 2p^2$ $^2S)$ $^2S_{0.5}$	7.797	4.18E-02		m
$1s^2\ 2s^1$ $^1S)$ $^2S_{0.5}$	$1s^1\ 2s^1\ 2p^1$ $^3S)$ $^2P_{0.5}$	7.807	3.20E-02	7.805	t
$1s^2\ 2s^1$ $^1S)$ $^2S_{0.5}$	$1s^1\ 2s^1\ 2p^1$ $^3S)$ $^2P_{1.5}$	7.806	4.04E-02		s
$1s^2\ 2s^1$ $^1S)$ $^2S_{0.5}$	$1s^1\ 2s^1\ 2p^1$ $^1S)$ $^2P_{0.5}$	7.849	2.28E-01	7.849	r
$1s^2\ 2s^1$ $^1S)$ $^2S_{0.5}$	$1s^1\ 2s^1\ 2p^1$ $^1S)$ $^2P_{1.5}$	7.846	4.79E-01		q
$1s^2\ 2p^1$ $^1S)$ $^2P_{0.5}$	$1s^1\ 2p^2$ $^2S)$ $^2P_{0.5}$	7.856	2.63E-01		d
$1s^2\ 2p^1$ $^1S)$ $^2P_{0.5}$	$1s^1\ 2p^2$ $^2S)$ $^2P_{1.5}$	7.853	8.73E-02		b
$1s^2\ 2p^1$ $^1S)$ $^2P_{1.5}$	$1s^1\ 2p^2$ $^2S)$ $^2P_{0.5}$	7.860	6.07E-02		–
$1s^2\ 2p^1$ $^1S)$ $^2P_{1.5}$	$1s^1\ 2p^2$ $^2S)$ $^2P_{1.5}$	7.856	3.37E-01		a
$1s^2\ 2p^1$ $^1S)$ $^2P_{0.5}$	$1s^1\ 2p^2$ $^2S)$ $^2D_{1.5}$	7.869	2.50E-01		k
$1s^2\ 2p^1$ $^1S)$ $^2P_{1.5}$	$1s^1\ 2p^2$ $^2S)$ $^2D_{2.5}$	7.873	1.87E-01	7.875	j
$1s^2\ 2p^1$ $^1S)$ $^2P_{0.5}$	$1s^1\ 2p^2$ $^2S)$ $^4P_{0.5}$	7.925	9.73E-05		i
$1s^2\ 2p^1$ $^1S)$ $^2P_{1.5}$	$1s^1\ 2p^2$ $^2S)$ $^4P_{1.5}$	7.927	1.18E-04		f
$1s^2\ 2p^1$ $^1S)$ $^2P_{1.5}$	$1s^1\ 2p^2$ $^2S)$ $^4P_{2.5}$	7.924	2.93E-04		e
$1s^2\ 2s^1$ $^1S)$ $^2S_{0.5}$	$1s^1\ 2s^1\ 2p^1$ $^3S)$ $^4P_{0.5}$	7.932	4.55E-05		v
$1s^2\ 2s^1$ $^1S)$ $^2S_{0.5}$	$1s^1\ 2s^1\ 2p^1$ $^3S)$ $^4P_{1.5}$	7.930	2.39E-04		u

Table 2.3. Strongest Be-Like K_α Transitions for Aluminum

		This calculation		M. Chen's Data	
Lower Level	Upper Level	Wavelength (Å)	f-value	Wavelength (Å)	f-value
$1s^2\ 2p^2$ $^1S)\ ^1D_{2.0}$	$1s^1\ 2p^3$ $^2S)\ ^1P_{1.0}$	7.909	1.22E-01	7.910	1.10E-01
$1s^2\ 2s^2$ $^1S)\ ^1S_{0.0}$	$1s^1\ 2s^2\ 2p^1$ $^2S)\ ^1P_{1.0}$	7.923	7.20E-01	7.923	6.88E-01
$1s^2\ 2s^1\ 2p^1$ $^2S)\ 1P_{1.0}$	$1s^1\ 2s^1\ 2p^2$ $^1S)\ ^1S_{0.0}$	7.925	4.22E-02	7.923	3.91E-02
$1s^2\ 2s^1\ 2p^1$ $^2S)\ ^1P_{1.0}$	$1s^1\ 2s^1\ 2p^2$ $^3S)\ ^1P_{1.0}$	7.931	3.67E-01	7.932	3.50E-01
$1s^2\ 2p^2$ $^1S)\ ^1D_{2.0}$	$1s^1\ 2p^3$ $^2S)\ ^1D_{2.0}$	7.957	3.16E-01	7.961	3.00E-01
$1s^2\ 2p^2$ $^1S)\ ^1S_{0.0}$	$1s^1\ 2p^3$ $^2S)\ ^1P_{1.0}$	7.972	4.97E-01	7.979	4.74E-01
$1s^2\ 2s^1\ 2p^1$ $^2S)\ ^1P_{1.0}$	$1s^1\ 2s^1 2p^2$ $^1S)\ ^1D_{2.0}$	7.973	1.98E-01	7.975	1.83E-01
$1s^2\ 2s^1\ 2p^1$ $^2S)\ ^3P_{0.0}$	$1s^1\ 2s^1\ 2p^2$ $^2S)\ ^3S_{1.0}$	7.895	3.66E-02		
$1s^2\ 2s^1\ 2p^1$ $^2S)\ ^3P_{1.0}$	$1s^1\ 2s^1\ 2p^2$ $^2S)\ ^3S_{1.0}$	7.896	3.88E-02		
$1s^2\ 2s^1\ 2p^1$ $^2S)\ ^3P_{2.0}$	$1s^1\ 2s^1\ 2p^2$ $^2S)\ ^3S_{1.0}$	7.899	4.29E-02		
$1s^2\ 2p^2$ $^1S)\ ^3P_{0.0}$	$1s^1\ 2p^3$ $^2S)\ ^3P_{1.0}$	7.922	9.04E-02		
$1s^2\ 2p^2$ $^1S)\ ^3P_{1.0}$	$1s^1\ 2p^3$ $^2S)\ ^3P_{1.0}$	7.924	2.40E-02		
$1s^2\ 2p^2$ $^1S)\ ^3P_{1.0}$	$1s^1\ 2p^3$ $^2S)\ ^3P_{2.0}$	7.923	3.55E-02		
$1s^2\ 2p^2$ $^1S)\ ^3P_{2.0}$	$1s^1\ 2p^3$ $^2S)\ ^3P_{1.0}$	7.926	3.81E-02		
$1s^2\ 2p^2$ $^1S)\ ^3P_{2.0}$	$1s^1\ 2p^3$ $^2S)\ ^3P_{2.0}$	7.925	7.32E-02		
$1s^2\ 2s^1\ 2p^1$ $^2S)\ ^3P_{0.0}$	$1s^1\ 2s^1\ 2p^2$ $^1S)\ ^3P_{1.0}$	7.943	5.37E-01		
$1s^2\ 2s^1\ 2p^1$ $^2S)\ ^3P_{1.0}$	$1s^1\ 2s^1\ 2p^2$ $^1S)\ ^3P_{0.0}$	7.946	1.18E-01		
$1s^2\ 2s^1\ 2p^1$ $^2S)\ ^3P_{1.0}$	$1s^1\ 2s^1\ 2p^2$ $^1S)\ ^3P_{1.0}$	7.945	3.60E-02		
$1s^2\ 2s^1\ 2p^1$ $^2S)\ ^3P_{1.0}$	$1s^1\ 2s^1\ 2p^2$ $^1S)\ ^3P_{2.0}$	7.942	4.20E-03		
$1s^2\ 2s^1\ 2p^1$ $^2S)\ ^3P_{2.0}$	$1s^1\ 2s^1\ 2p^2$ $^1S)\ ^3P_{1.0}$	7.947	6.23E-02		
$1s^2\ 2s^1\ 2p^1$ $^2S)\ ^3P_{2.0}$	$1s^1\ 2s^1\ 2p^2$ $^1S)\ ^3P_{2.0}$	7.943	2.63E-01		
$1s^2\ 2s^1\ 2p^1$ $^2S)\ ^3P_{0.0}$	$1s^1\ 2s^1\ 2p^2$ $^3S)\ ^3D_{1.0}$	7.942	2.81E-02		
$1s^2\ 2s^1\ 2p^1$ $^2S)\ ^3P_{1.0}$	$1s^1\ 2s^1\ 2p^2$ $^3S)\ ^3D_{1.0}$	7.943	1.06E-01		
$1s^2\ 2s^1\ 2p^1$ $^2S)\ ^3P_{1.0}$	$1s^1\ 2s^1\ 2p^2$ $^3S)\ ^3D_{2.0}$	7.944	2.95E-01		
$1s^2\ 2s^1\ 2p^1$ $^2S)\ ^3P_{2.0}$	$1s^1\ 2s^1\ 2p^2$ $^3S)\ ^3D_{1.0}$	7.945	2.47E-02		
$1s^2\ 2s^1\ 2p^1$ $^2S)\ ^3P_{2.0}$	$1s^1\ 2s^1\ 2p^2$ $^3S)\ ^3D_{2.0}$	7.946	3.41E-02		
$1s^2\ 2s^1\ 2p^1$ $^2S)\ ^3P_{2.0}$	$1s^1\ 2s^1\ 2p^2$ $^3S)\ ^3D_{3.0}$	7.945	1.67E-01		
$1s^2\ 2p^2$ $^1S)\ ^3P_{0.0}$	$1s^1\ 2p^3$ $^2S)\ ^3S_{1.0}$	7.957	1.82E-01		
$1s^2\ 2p^2$ $^1S)\ ^3P_{1.0}$	$1s^1\ 2p^3$ $^2S)\ ^3S_{1.0}$	7.958	1.78E-01		
$1s^2\ 2p^2$ $^1S)\ ^3P_{2.0}$	$1s^1\ 2p^3$ $^2S)\ ^3S_{1.0}$	7.960	1.60E-01		
$1s^2\ 2p^2$ $^1S)\ ^3P_{0.0}$	$1s^1\ 2p^3$ $^2S)\ ^3D_{1.0}$	7.970	2.10E-01		
$1s^2\ 2p^2$ $^1S)\ ^3P_{1.0}$	$1s^1\ 2p^3$ $^2S)\ ^3D_{1.0}$	7.971	4.54E-02		
$1s^2\ 2p^2$ $^1S)\ ^3P_{1.0}$	$1s^1\ 2p^3$ $^2S)\ ^3D_{2.0}$	7.971	1.55E-01		
$1s^2\ 2p^2$ $^1S)\ ^3P_{2.0}$	$1s^1\ 2p^3$ $^2S)\ ^3D_{1.0}$	7.973	1.67E-03		
$1s^2\ 2p^2$ $^1S)\ ^3P_{2.0}$	$1s^1\ 2p^3$ $^2S)\ ^3D_{2.0}$	7.973	2.46E-02		
$1s^2\ 2p^2$ $^1S)\ ^3P_{2.0}$	$1s^1\ 2p^3$ $^2S)\ ^3D_{3.0}$	7.973	1.64E-01		

Table 2.4. Strongest B-Like K_α Transitions for Aluminum

Lower Level	Upper Level	Wavelength (Å)	f-value
$1s^2\ 2s^1\ 2p^2\quad {}^2S)\ {}^2D_{1.5}$	$1s^1\ 2s^1\ 2p^3\quad {}^1S)\ {}^2P_{1.5}$	8.009	3.09E-02
$1s^2\ 2s^1\ 2p^2\quad {}^2S)\ {}^2D_{1.5}$	$1s^1\ 2s^1\ 2p^3\quad {}^1S)\ {}^2P_{0.5}$	8.008	9.45E-02
$1s^2\ 2s^1\ 2p^2\quad {}^2S)\ {}^2D_{2.5}$	$1s^1\ 2s^1\ 2p^3\quad {}^1S)\ {}^2P_{1.5}$	8.009	1.00E-01
$1s^2\ 2s^1\ 2p^2\quad {}^2S)\ {}^4P_{0.5}$	$1s^1\ 2s^1\ 2p^3\quad {}^3S)\ {}^4P_{0.5}$	8.008	1.71E-02
$1s^2\ 2s^1\ 2p^2\quad {}^2S)\ {}^4P_{0.5}$	$1s^1\ 2s^1\ 2p^3\quad {}^3S)\ {}^4P_{1.5}$	8.008	7.86E-02
$1s^2\ 2s^1\ 2p^2\quad {}^2S)\ {}^4P_{1.5}$	$1s^1\ 2s^1\ 2p^3\quad {}^3S)\ {}^4P_{0.5}$	8.009	5.11E-02
$1s^2\ 2s^1\ 2p^2\quad {}^2S)\ {}^4P_{1.5}$	$1s^1\ 2s^1\ 2p^3\quad {}^3S)\ {}^4P_{2.5}$	8.009	4.34E-02
$1s^2\ 2s^1\ 2p^2\quad {}^2S)\ {}^4P_{1.5}$	$1s^1\ 2s^1\ 2p^3\quad {}^3S)\ {}^4P_{1.5}$	8.009	1.52E-02
$1s^2\ 2s^1\ 2p^2\quad {}^2S)\ {}^4P_{2.5}$	$1s^1\ 2s^1\ 2p^3\quad {}^3S)\ {}^4P_{2.5}$	8.011	9.04E-02
$1s^2\ 2s^1\ 2p^2\quad {}^2S)\ {}^4P_{2.5}$	$1s^1\ 2s^1\ 2p^3\quad {}^3S)\ {}^4P_{1.5}$	8.011	4.35E-02
$1s^2\ 2s^2\ 2p^1\quad {}^1S)\ {}^2P_{0.5}$	$1s^1\ 2s^2\ 2p^2\quad {}^2S)\ {}^2P_{0.5}$	8.013	2.53E-01
$1s^2\ 2s^2\ 2p^1\quad {}^1S)\ {}^2P_{0.5}$	$1s^1\ 2s^2\ 2p^2\quad {}^2S)\ {}^2P_{1.5}$	8.009	7.77E-02
$1s^2\ 2s^2\ 2p^1\quad {}^1S)\ {}^2P_{1.5}$	$1s^1\ 2s^2\ 2p^2\quad {}^2S)\ {}^2P_{0.5}$	8.016	4.63E-02
$1s^2\ 2s^2\ 2p^1\quad {}^1S)\ {}^2P_{1.5}$	$1s^1\ 2s^2\ 2p^2\quad {}^2S)\ {}^2P_{1.5}$	8.012	3.05E-01
$1s^2\ 2s^1\ 2p^2\quad {}^2S)\ {}^2P_{0.5}$	$1s^1\ 2s^1\ 2p^3\quad {}^3S)\ {}^2S_{\ 0.5}$	8.019	9.54E-02
$1s^2\ 2s^1\ 2p^2\quad {}^2S)\ {}^2P_{1.5}$	$1s^1\ 2s^1\ 2p^3\quad {}^3S)\ {}^2S_{\ 0.5}$	8.021	1.79E-01
$1s^2\ 2p^3\quad {}^1S)\ {}^2D_{1.5}$	$1s^1\ 2p^4\quad {}^2S)\ {}^2P_{1.5}$	8.021	1.64E-02
$1s^2\ 2p^3\quad {}^1S)\ {}^2D_{1.5}$	$1s^1\ 2p^4\quad {}^2S)\ {}^2P_{0.5}$	8.019	1.41E-01
$1s^2\ 2p^3\quad {}^1S)\ {}^2D_{2.5}$	$1s^1\ 2p^4\quad {}^2S)\ {}^2P_{1.5}$	8.021	1.88E-01
$1s^2\ 2s^2\ 2p^1\quad {}^1S)\ {}^2P_{0.5}$	$1s^1\ 2s^2\ 2p^2\quad {}^2S)\ {}^2D_{1.5}$	8.022	2.27E-01
$1s^2\ 2s^2\ 2p^1\quad {}^1S)\ {}^2P_{1.5}$	$1s^1\ 2s^2\ 2p^2\quad {}^2S)\ {}^2D_{1.5}$	8.025	3.88E-03
$1s^2\ 2s^2\ 2p^1\quad {}^1S)\ {}^2P_{1.5}$	$1s^1\ 2s^2\ 2p^2\quad {}^2S)\ {}^2D_{2.5}$	8.025	1.69E-01

Table 2.4 (Continued)

Lower Level	Upper Level	Wavelength (Å)	f-value
$1s^2\ 2p^3$ $^1S)\ ^2D_{1.5}$	$1s^1\ 2p^4$ $^2S)\ ^2D_{1.5}$	8.033	1.77E-01
$1s^2\ 2p^3$ $^1S)\ ^2D_{1.5}$	$1s^1\ 2p^4$ $^2S)\ ^2D_{2.5}$	8.031	1.29E-02
$1s^2\ 2p^3$ $^1S)\ ^2D_{2.5}$	$1s^1\ 2p^4$ $^2S)\ ^2D_{1.5}$	8.033	1.47E-03
$1s^2\ 2p^3$ $^1S)\ ^2D_{2.5}$	$1s^1\ 2p^4$ $^2S)\ ^2D_{2.5}$	8.031	1.58E-01
$1s^2\ 2s^1\ 2p^2$ $^2S)\ ^4P_{0.5}$	$1s^1\ 2s^1\ 2p^3$ $^1S)\ ^4S_{1.5}$	8.036	1.62E-01
$1s^2\ 2s^1\ 2p^2$ $^2S)\ ^4P_{1.5}$	$1s^1\ 2s^1\ 2p^3$ $^1S)\ ^4S_{1.5}$	8.037	1.69E-01
$1s^2\ 2s^1\ 2p^2$ $^2S)\ ^4P_{2.5}$	$1s^1\ 2s^1\ 2p^3$ $^1S)\ ^4S_{1.5}$	8.039	1.51E-01
$1s^2\ 2s^1\ 2p^2$ $^2S)\ ^2D_{1.5}$	$1s^1\ 2s^1\ 2p^3$ $^1S)\ ^2D_{1.5}$	8.040	2.85E-01
$1s^2\ 2s^1\ 2p^2$ $^2S)\ ^2D_{1.5}$	$1s^1\ 2s^1\ 2p^3$ $^1S)\ ^2D_{2.5}$	8.039	3.34E-02
$1s^2\ 2s^1\ 2p^2$ $^2S)\ ^2D_{2.5}$	$1s^1\ 2s^1\ 2p^3$ $^1S)\ ^2D_{1.5}$	8.040	2.47E-02
$1s^2\ 2s^1\ 2p^2$ $^2S)\ ^2D_{2.5}$	$1s^1\ 2s^1\ 2p^3$ $^1S)\ ^2D_{2.5}$	8.039	3.02E-01
$1s^2\ 2s^1\ 2p^2$ $^2S)\ ^4P_{0.5}$	$1s^1\ 2s^1\ 2p^3$ $^3S)\ ^4D_{1.5}$	8.039	1.14E-01
$1s^2\ 2s^1\ 2p^2$ $^2S)\ ^4P_{0.5}$	$1s^1\ 2s^1\ 2p^3$ $^3S)\ ^4D_{0.5}$	8.039	9.86E-02
$1s^2\ 2s^1\ 2p^2$ $^2S)\ ^4P_{1.5}$	$1s^1\ 2s^1\ 2p^3$ $^3S)\ ^4D_{1.5}$	8.041	5.21E-02
$1s^2\ 2s^1\ 2p^2$ $^2S)\ ^4P_{1.5}$	$1s^1\ 2s^1\ 2p^3$ $^3S)\ ^4D_{2.5}$	8.041	1.310E-01
$1s^2\ 2s^1\ 2p^2$ $^2S)\ ^4P_{2.5}$	$1s^1\ 2s^1\ 2p^3$ $^3S)\ ^4D_{1.5}$	8.042	3.88E-03
$1s^2\ 2s^1\ 2p^2$ $^2S)\ ^4P_{2.5}$	$1s^1\ 2s^1\ 2p^3$ $^3S)\ ^4D_{2.5}$	8.042	2.77E-02
$1s^2\ 2s^1\ 2p^2$ $^2S)\ ^4P_{2.5}$	$1s^1\ 2s^1\ 2p^3$ $^3S)\ ^4D_{3.5}$	8.042	1.53E-01
$1s^2\ 2p^3$ $^1S)\ ^4S)_{1.5}$	$1s^1\ 2p^4$ $^2S)\ ^4P_{2.5}$	8.044	1.66E-01
$1s^2\ 2p^3$ $^1S)\ ^4S_{1.5}$	$1s^1\ 2p^4$ $^2S)\ ^4P_{1.5}$	8.042	1.11E-01

irradiated with a second beam to provide a backlighting source in the Al K_α spectral regime ($h\nu \approx 1.5$ keV). In the PBFA-II experiments K_α emission lines are produced as $2p$ electrons drop down to fill $1s$ vacancies created by the ion beam. It is important to note that emission and absorption K_α spectroscopy provide different types of information about the state of the plasma. That is, absorption spectroscopy provides a direct measure of the population of the *lower* state of a bound-bound transition, while emission spectroscopy measures the *upper* state. Comparisons with the laser-plasma measurements are also useful because the spectral resolution in the experiments was about a factor of 2 greater than in the PBFA-II experiments, thus allowing for easier line identification.

Comparison of our new calculations with the K_α absorption spectra of Perry et al. (1991) are shown in Fig. 2.4. In the calculations, we assumed the target to be planar with an original (pre-expansion) thickness of $\Delta L_{\rm orig} = 500$ Å. The plasma conditons were $T = 58$ eV and $\rho = 0.02$ g/cm^3. The computed absorption spectrum was convolved with a Gaussian of FWHM = 0.6 eV to account for the instrumental spectral resolution. Note that overall the calculated spectrum is in good agreement with this experimental spectrum, particularly when one considers the sensitivity of the spectrum to the plasma temperature and density (see, e.g., Figs. 3 and 5 of Section 3).

The mn and st satellites of Li-like Al ($\lambda = 7.795$ Å and 7.807 Å, respectively) are now in better agreement with the Perry et al. data than in our previous calculations, with the errors in the calculated wavelengths being $\lesssim$ a few mÅ. The calculated wavelengths for the other major Li-like features at 7.846 Å (qr), 7.855 Å (bda), and 7.870 Å (kj) are in good agreement with both the Perry et al. and Boiko et al. (1978) experimental wavelengths. (See Tables 2.2 through 2.4 for transition identification.)

The absorption strengths of the calculated features agree reasonably well with the experimental spectrum. However, there are some discrepancies. The strengths of the Li-like mn and kj feature are not quite as deep as the Perry et al. data. This is probably not a problem with the calculated ionization balance, however, because the He-like and B-like features have approximately the right depth. It could perhaps be due to transitions involving highly excited states which are absent in our atomic model. The Be-like transitions $1s^2 2s^1 2p^1\ ^3P \rightarrow 1s^1 2s^1 2p^2\ ^3P$ which are blended with the Li-like kj lines are included in our model. On the other hand, our model involving K_β transitions ($1s \rightarrow 3p$) is less complete. However, we cannot say with certainty that this is the cause of the discrepancy.

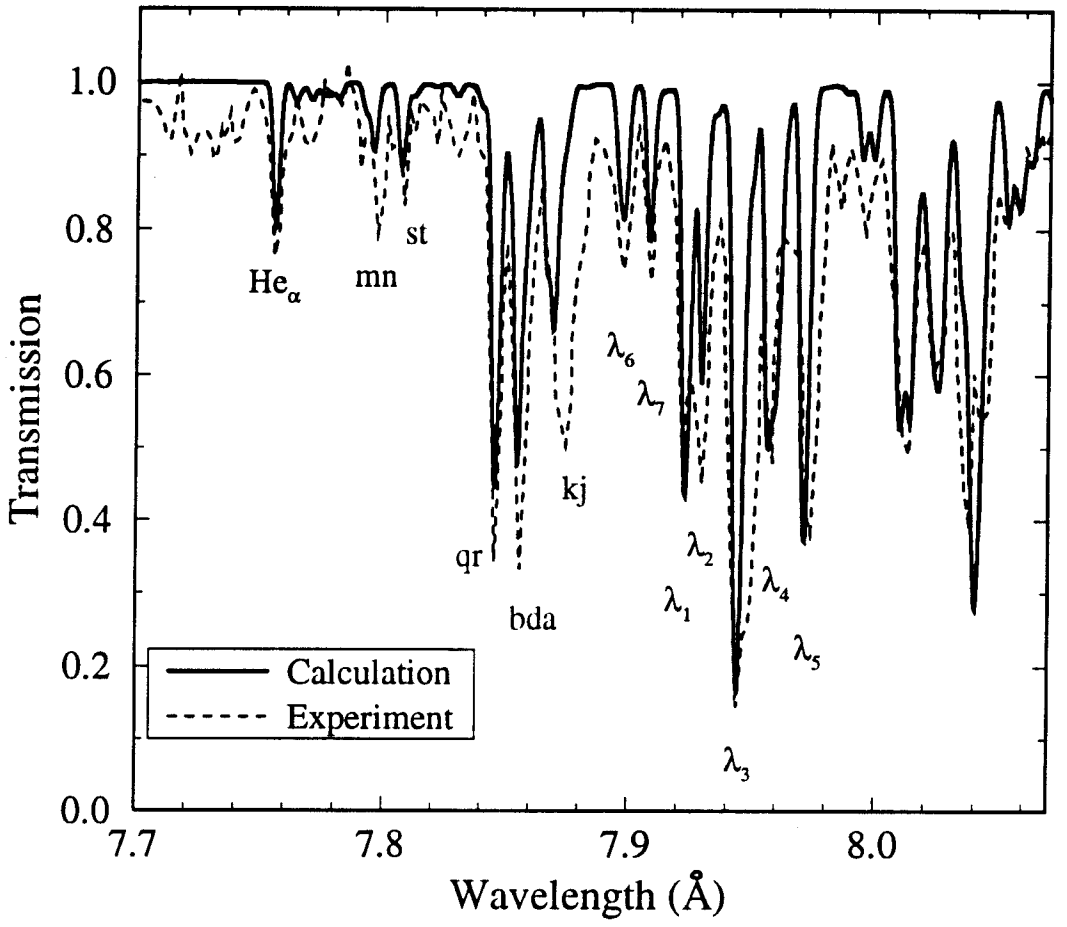

Figure 2.4. Comparison of calculated (solid curve) and experimental (dotted curve) K_α satellite absorption spectra for Al. Absorption features from He-like (He_α), Li-like (labelled *mn* through *kj*), Be-like (λ = 7.89-7.98 Å), and B-like (λ = 7.98-8.07 Å) aluminum are clearly seen.

The Be-like region shows 5 deep absorption features between 7.92 Å and 7.98 Å. The strongest central feature at $\lambda \approx 7.940 - 7.945$ Å is due to a combination of $1s^2 2s^1 2p^1\,{}^3P \rightarrow 1s^1 2s^1 2p^2\,{}^3P$ and $1s^2 2s^1 2p^1\,{}^3P \rightarrow 1s^1 2s^1 2p^2\,{}^3D$ transitions. Again, the agreement between the calculated and experimental spectra is good both in regard to the line positions and absorption depths.

The B-like satellites are seen between 7.98 Å and 8.05 Å. Three distinct peaks are seen both in the calculation and the Perry et al. data, with the feature near 8.04 Å showing hints of being resolved into distinct components (dotted line). In our calculations this feature has caused several ($\sim$ 10) strong transitions of the type $1s^2 2s^1 2p^2 \rightarrow 1s^1 2s^1 2p^3$ ($^4P \rightarrow {}^4D$, $^2D \rightarrow {}^2D$, and $^4P \rightarrow {}^4S$). Certainly, the atomic physics becomes more complex for the lower ionization stages as more lines can contribute to a single spectral feature seen in the data. Nevertheless, our good agreement with the Perry et al. and Boiko et al. data, as well as with the calculations by Chen and Iglesias, suggest that our identification of K_α emission lines in the PBFA-II spectra should be reliable. This is particularly true for Be-like and higher ionization stages of Al.

Figure 2.5 compares results of a calculated emission spectrum and the measured spectrum from PBFA-II Shot 5881. The calculations were performed for a plasma with $T = 40$ eV, $n = 10^{20}$ cm^3, and $L = 120$ (original foil thickness = 0.2 μm), and assume an instrumental resolution of $\lambda/\Delta\lambda = 1200$. In comparing the 2 spectra it is important to note that the measured spectrum is time-integrated. Thus, the photons from the B-like satellites (and lower ionization stages) were very likely emitted at times when the plasma temperature was lower. It can be seen in this figure that the calculated He-, Li-, and Be-like satellites line up very well with the emission peaks in the PBFA-II spectrum. We thus feel confident that the peak features in PBFA-II Al K_α spectrum are now correctly identified. This allows us to utilize the intensity ratios of K_α emission lines to diagnose target plasma conditions (see Section 2.D).

2.C. Temperature and Density Dependence of K_α Emission and Absorption Spectra

K_α emission and absorption spectra were computed over a range of temperatures and densities relevant to PBFA-II target plasma conditions. Figures 2.6 through 2.9 show the computed absorption (bottom) and emission (top) spectra for each temperature and density grid point. In each case, we assumed a monoenergetic beam of 9 MeV Li^{+3} ions with a power density of 3 TW/cm^2. The Al foil (pre-expansion) thickness was 2000 Å.

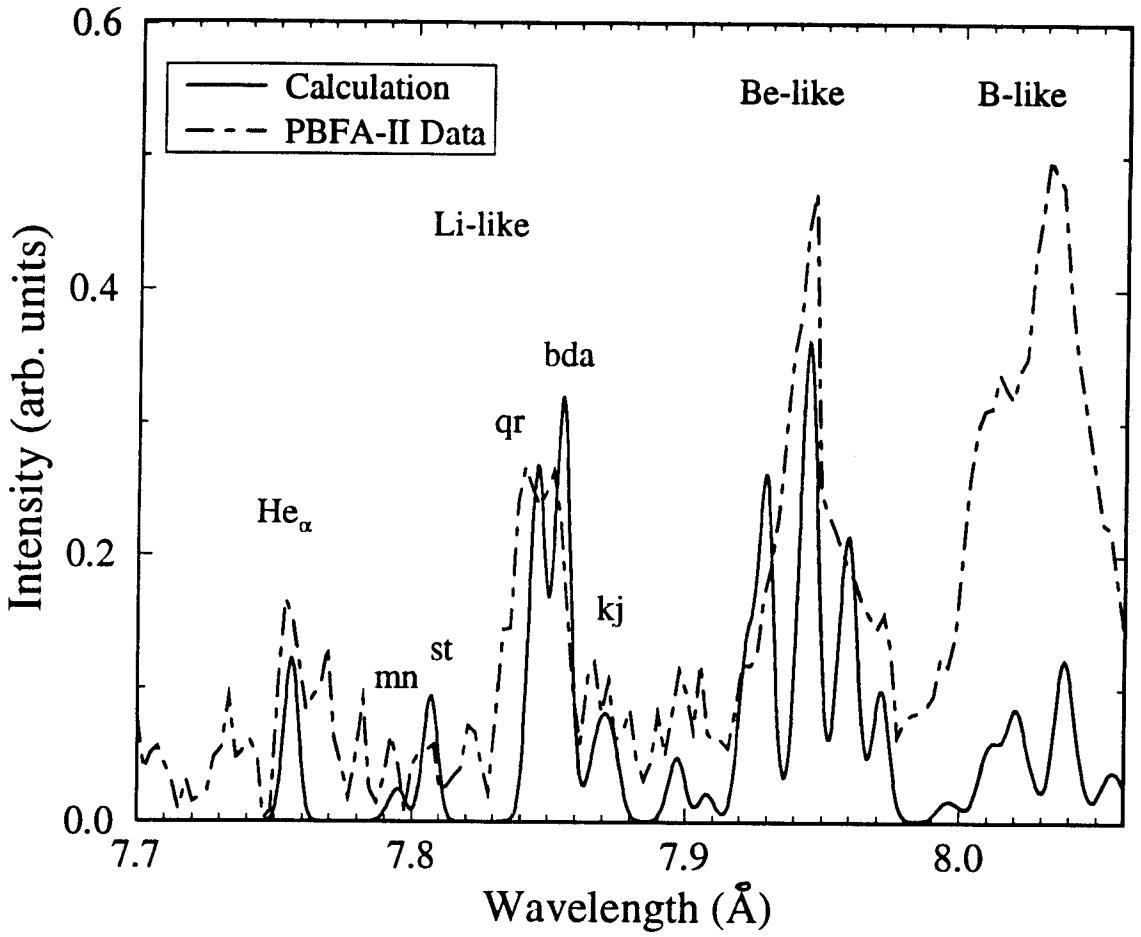

Figure 2.5. Comparison of PBFA-II spectrum from Shot 5881 with calculated spectrum for an Al plasma at $T = 40$ eV, $n = 10^{20}$ ions/cm^3, and $L = 120\,\mu$m.

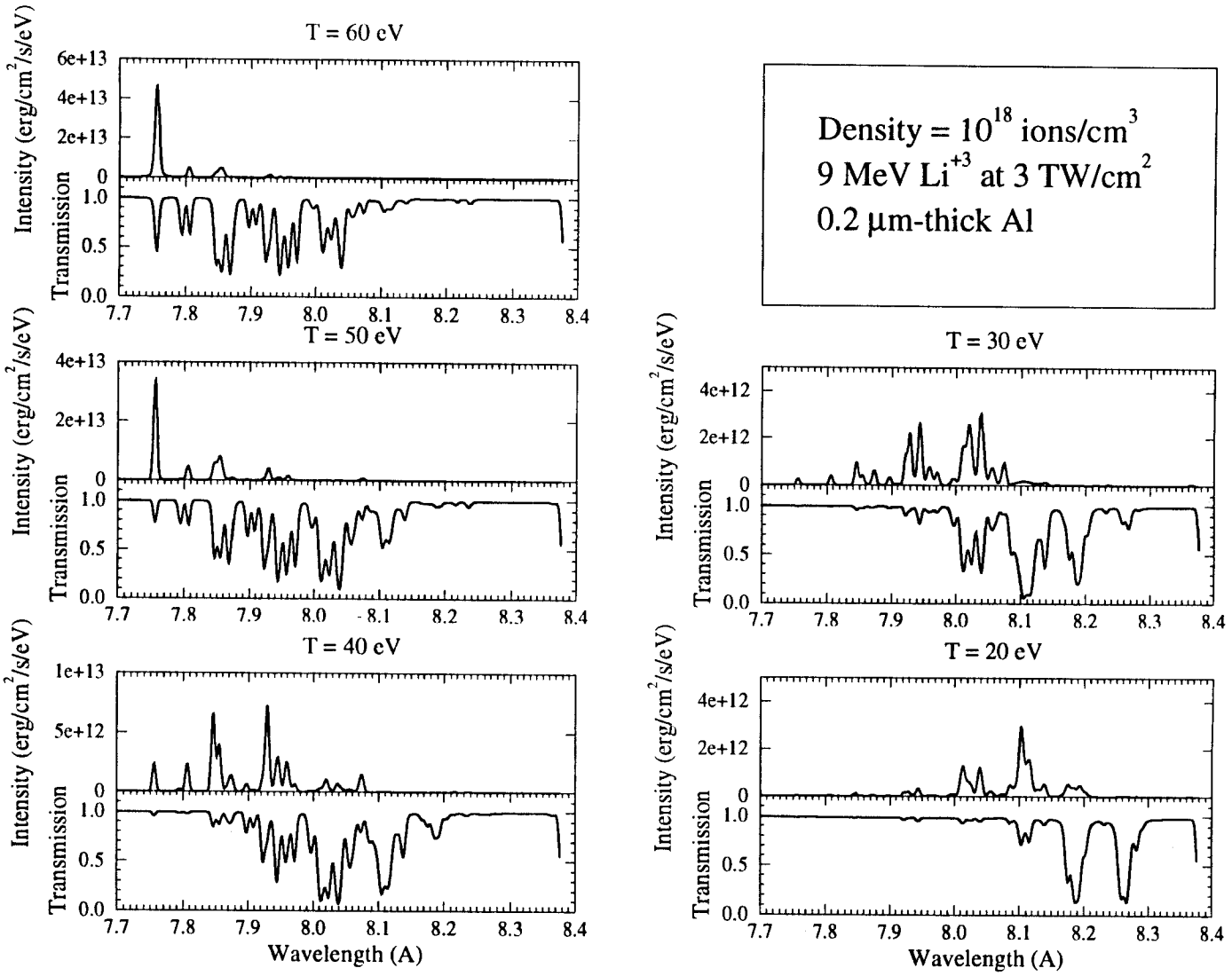

Figure 2.6. Calculated K_α emission and absorption spectra for Al plasmas at $n = 10^{18}$ ions/cm^3, and $L = 12$ mm.

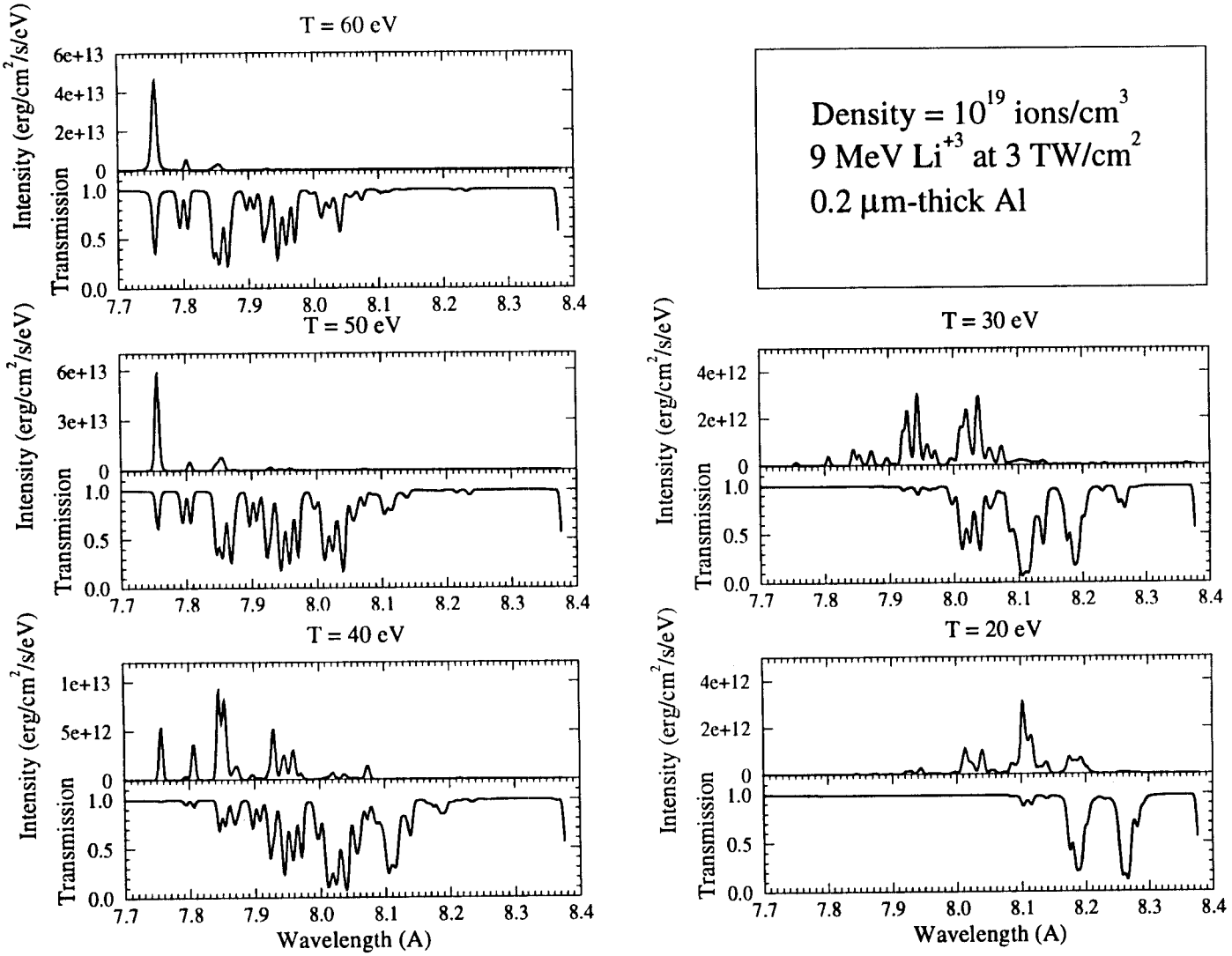

Figure 2.7. Calculated K_α emission and absorption spectra for Al plasmas at $n = 10^{19}$ ions/cm^3, and $L = 1.2$ mm.

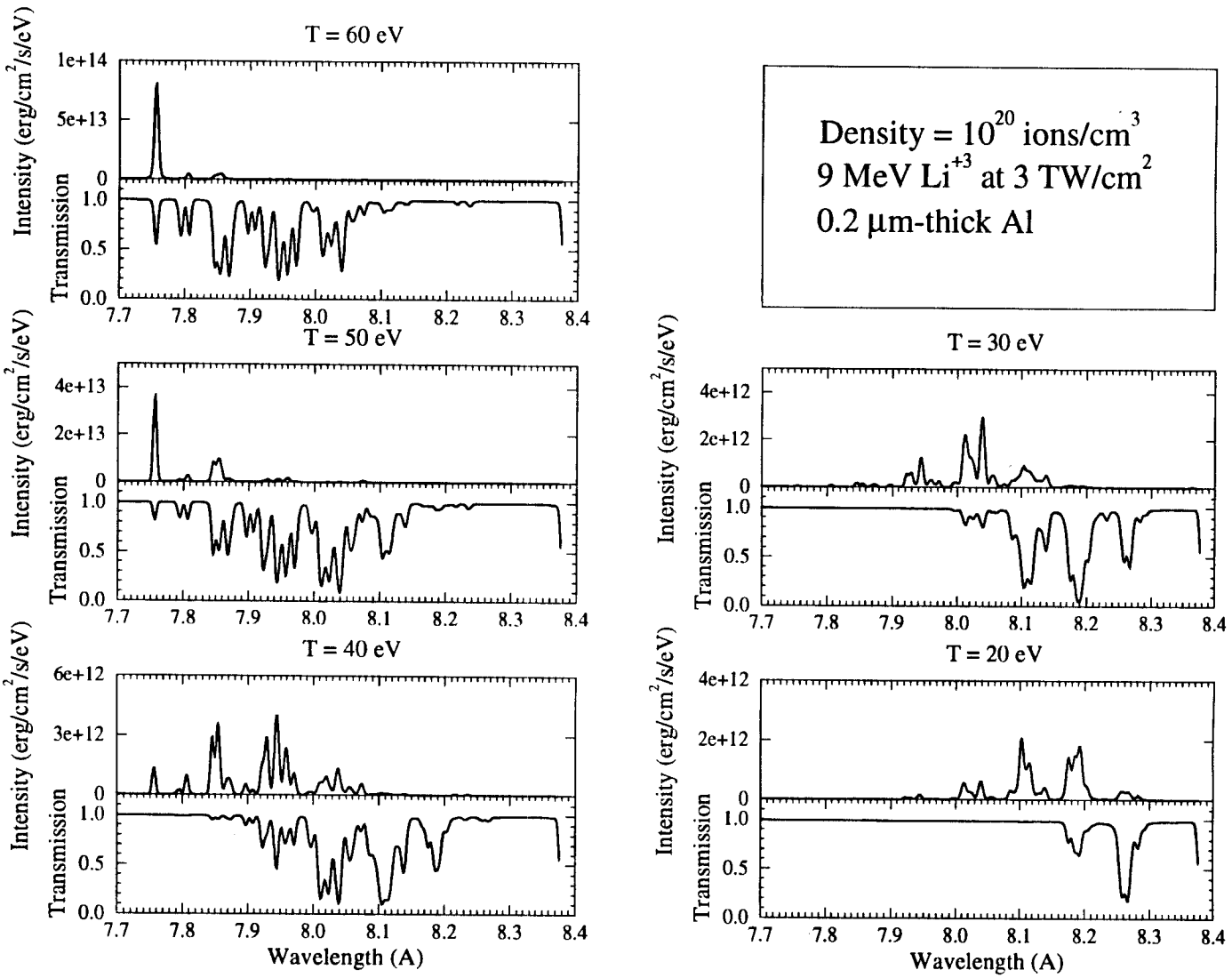

Figure 2.8. Calculated K_α emission and absorption spectra for Al plasmas at $n = 10^{20}$ ions/cm^3, and $L = 120\,\mu$m.

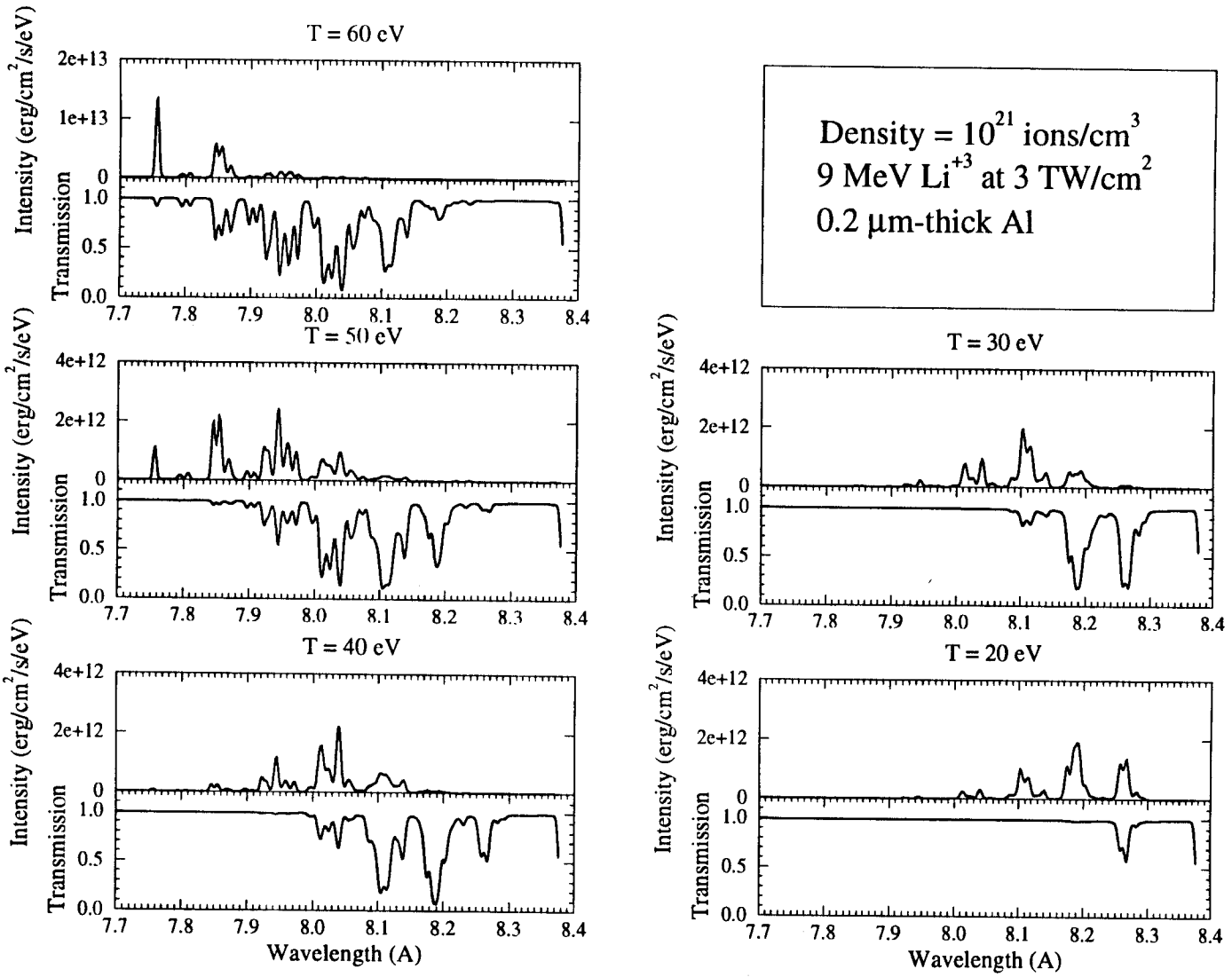

Figure 2.9. Calculated K_α emission and absorption spectra for Al plasmas at $n = 10^{21}$ ions/cm^3, and $L = 12\,\mu$m.

Results are shown for temperatures ranging from 20 eV to 60 eV, while ion densities range from $10^{18} - 10^{21}$ cm^3.

From the absorption spectra, which provides a more direct measure of the state of the bulk plasma, a shift to higher ionization is readily seen as the plasma temperature increases and/or the density decreases. It is also seen that the flux in the He_α line increases dramatically at temperatures above 50 eV, which we have discussed earlier (MacFarlane and Wang 1993). At $T = 60$ eV and $n = 10^{20}$ cm^{-3}, the intensity is approximately 8×10^{13} erg/cm^2/s/eV, which is more than an order of magnitude greater than the peak K_α fluxes from lower ionization stages of Al. It is also interesting to note that the Planck (blackbody) flux at this wavelength for a plasma at $T = 60$ eV is 3×10^4 erg/cm^2/s/eV. Thus, the maximum possible flux for the He_α line in the absence of the ion beam is more than 9 orders of magnitude lower than the flux when the ion beam is included.

Note that the K_α emission spectra are very sensitive to temperature. This can be more conveniently seen in Fig. 3 of Section 3, where results at different temperatures are shown in increments of 3 eV. For instance, at $T = 46$ eV peak the He_α line intensity $\lambda = 7.757$ Å) is approximately equivalent to the Li-like *qr* and *bda* lines near 7.85 Å. However, at $T = 43$ eV, the He_α intensity is only about half as high. This sensitivity is exploited in the next section to determine plasma conditions from K_α line intensity ratios.

Figure 2.10 shows that K_β transitions could potentially be observed in absorption, but are very weak in emission. The K_β absorption lines reside at shorter wavelengths ($6.6 < \lambda < 8.0$ Å) than the K_α lines and are not as deep. However, the depths can be increased by using thicker tracer layers. If K-shell absorption spectroscopy could also be performed in PBFA-II experiments, it could provide additional data for constraining plasma conditions.

2.D. Diagnosing Target Plasma Conditions from Line Intensity Ratios of K_α Emission Lines

In this section, we show how target plasma conditions can be accurately determined by examing the intensity ratios of K_α emission lines. Determining plasma temperatures within beam-heated targets is critical because it provides information about energy deposition and transport processes. Utilizing inner-shell x-ray lines has the advantage that conditions deeper with the target can be probed due to reduced

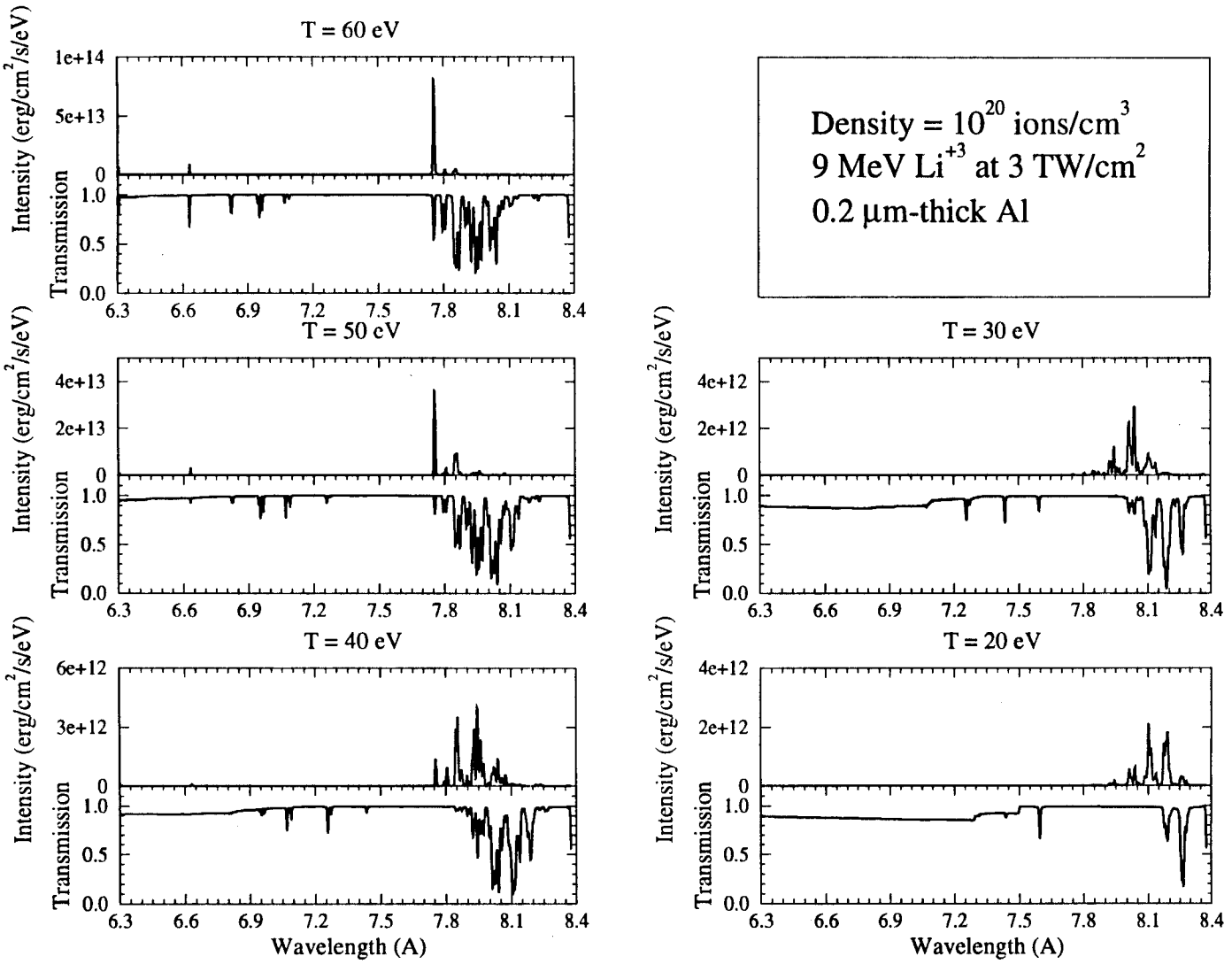

Figure 2.10. Calculated K_α and K_β emission and absorption spectra for Al plasmas at $n = 10^{20}$ ions/cm^3, and $L = 120\,\mu$m.

attenuation effects at shorter wavelengths. Here, we apply this technique to the analysis of Al K_α spectra obtained from PBFA-II Li beam experiments performed in early 1993.

In our analysis, emission spectra are computed for plasmas over a grid of temperatures and densities relevant to the K_α "plastic sandwich" experiments. In each case the plasmas were spatially uniform with a thickness corresponding to a pre-expansion foil thickness of 2000 Å. Thus, radiative transfer (including resonance self-absorption) effects were included.

In these calculations, we focus in particular on the K_α lines of He-, Li-, and Be-like lines. Atomic levels involved in the K_α transitions include fine-structure splitting. Multiple ionization effects — that is, the simultaneous ejection of a K-shell and one or more L-shell electrons — induced by the Li^{3+} beam were also considered.

The synthetic spectra were post-processed in the following way. The emission flux was integrated over narrow frequency regions composed of either one or a small number of strong emission lines. For example, the intensity of the Li-like *st* lines ($\lambda_{\rm calc}(s) = 7.806$ Å; $\lambda_{\rm calc}(t) = 7.807$ Å) was obtained by integrating the flux between 7.802 and 7.812 Å. No other strong emission lines occur within this 10 mÅ interval. (The intensities are also cross-checked with line power densities calculated using frequency-integrated escape probabilities for each line.) It is important to note, however, that there can be considerable line overlap effects for the K_α satellites of relatively low ionization stages. This introduces additional complexity into the analysis when different transitions cannot be spectrally resolved (e.g., when some are temperature-sensitive and some are not). For this reason, we use the K_α line intensities from only the He-, Li-, and Be-like stages in our analysis. For experiments with different plasma conditions, the tracer composition can be tuned so that these relatively high ionization stages can be utilized.

Base Case

Figures 2.11 and 2.12 summarize the most significant results of these calculations. Figure 2.11 shows the intensity ratios of 3 Li-like K_α lines relative to the He_α line as a function of temperature. For each curve the density is held constant. Also shown in each of the 3 plots are the *preliminary* estimates of the observed ratios for Shot 5881. The observed values are indicated by the diffuse orange shading, which provide a very rough indication of the uncertainty in the observed value.

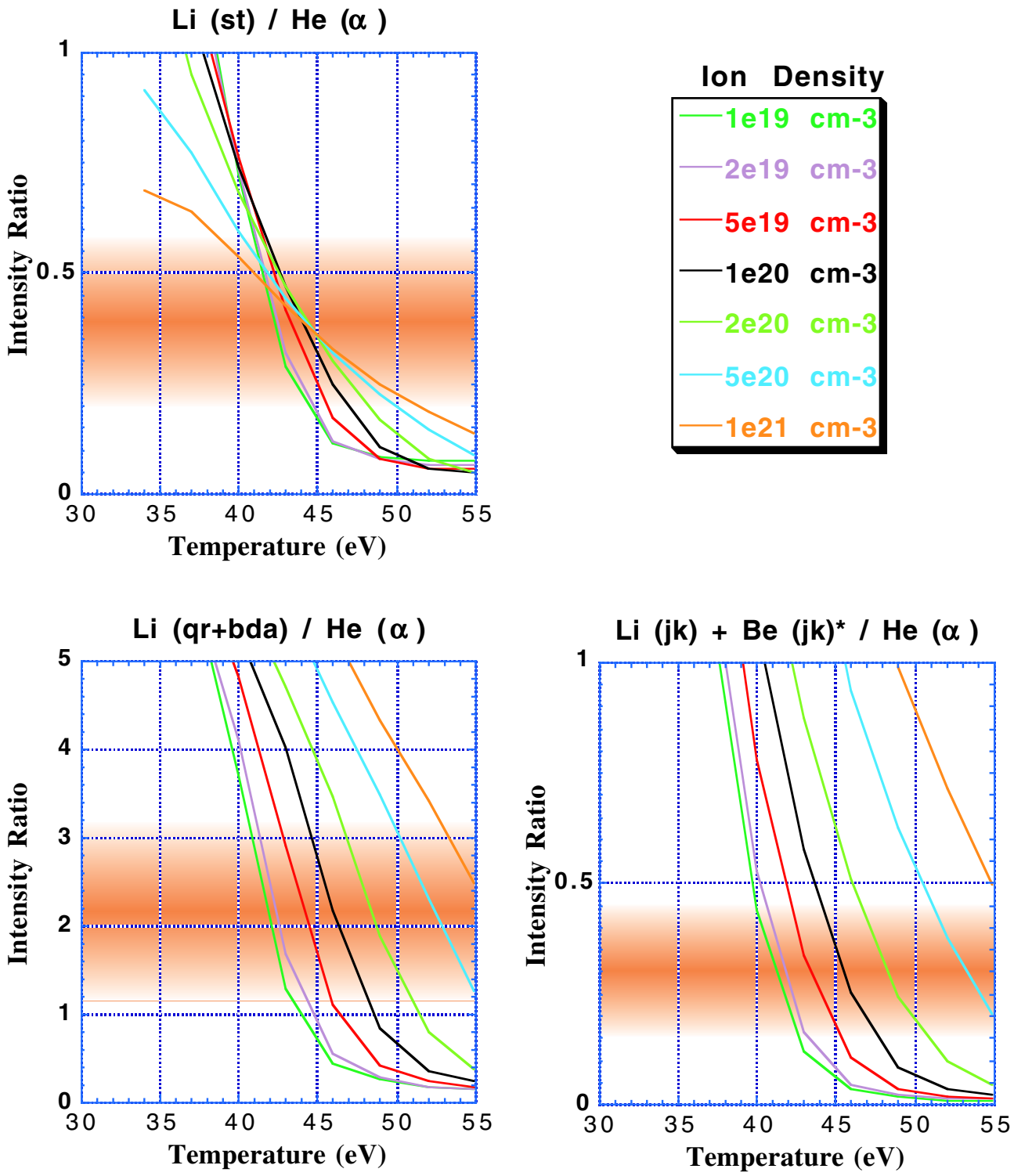

Figure 2.11. Temperature-sensitive K_α line intensity ratios. The shaded areas represent rough estimates of ratios measured in PBFA-II Shot 5881.

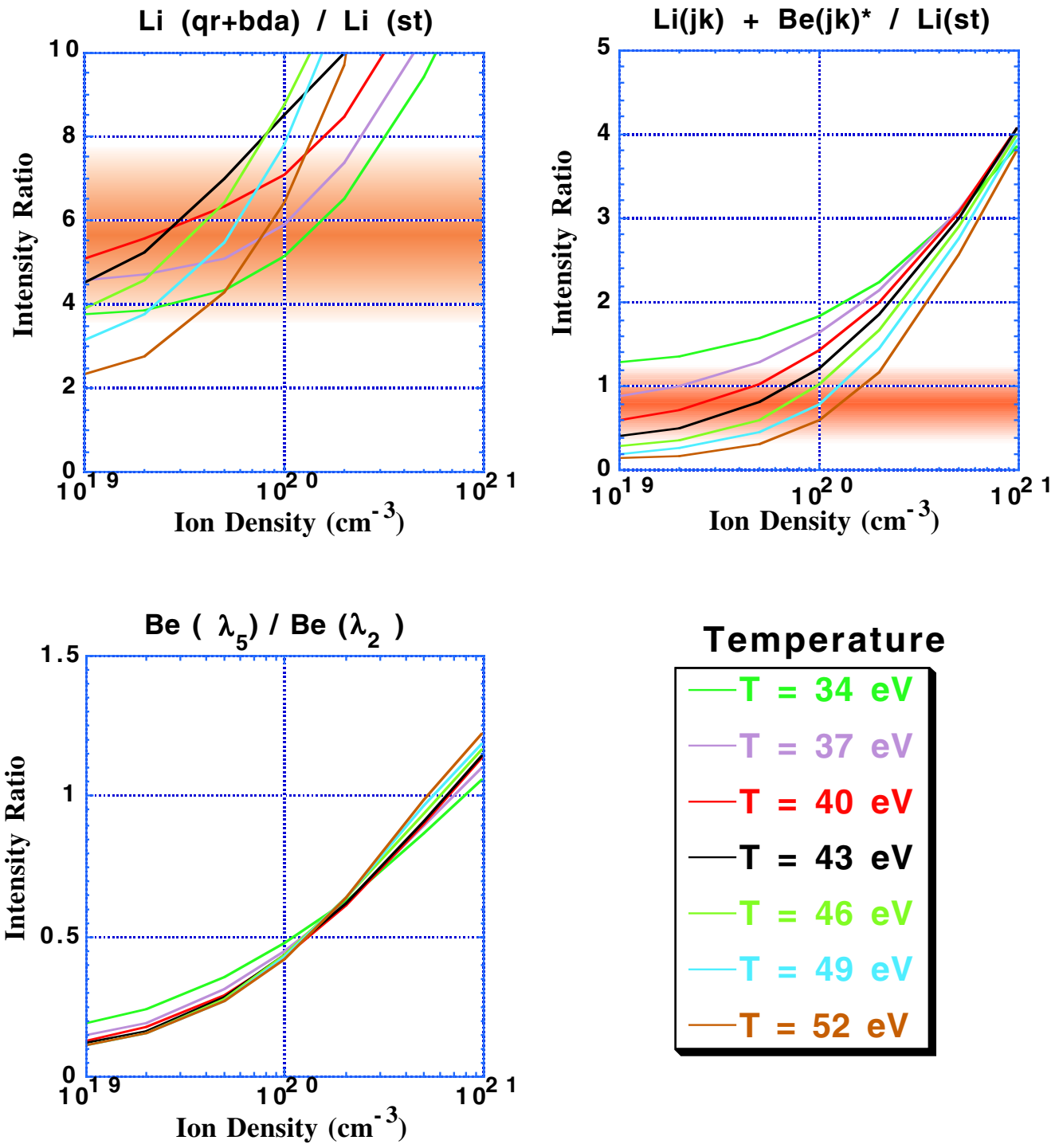

Figure 2.12 Density-sensitive K_α line intensity ratios. The shaded areas represent rough estimates of ratios measured in PBFA-II Shot 5881.

Note that the Li(st)/He$_\alpha$ ratio provides a very good temperature diagnostic. That is, the calculated intensity ratio is very sensitive to the temperature but relatively insensitive to the density for the plasma conditions of interest. Thus, for a measured intensity ratio of [Li(st)]/[He$_\alpha$] = 0.4, the plasma temperature is predicted to be $T = 42 - 45$ eV over the entire density range shown. The [Li($qr + bda$)]/[He$_\alpha$] and [Li(jk) + Be(jk)*]/[He$_\alpha$] are also sensitive to temperature, but show a greater dependence on the density than in the previous case. However, using results from radiative-hydrodynamics simulations as a guide, a density of $\rho \approx 10^{-3}\,\rho_{\rm solid}$ ($n = 6 \times 10^{19}$ ions/cm^3) is expected at the time at which the maximum plasma temperature is achieved. The temperatures inferred from the lower 2 plots in Fig. 2.11 using this density are $T = 44 - 45$ eV, which is consistent with that derived from the Li(st)/He$_\alpha$ ratio. In all cases, the temperature is restricted to a range between approximately 42 eV and 50 eV for the rather large density region between 1×10^{19} ions/cm^3 and 3×10^{20} ions/cm^3.

Information on the density can be obtained by examining the intensity ratios of lines within the same ionization stage. This is shown in Fig. 2.12 for two Li-like cases and one Be-like case. In Fig. 2.12 the intensity ratio is plotted as a function of density with the temperature held constant for each curve. The Be-like intensity ratio shows very good density sensitivity as the temperature dependence is relatively weak. For the Li-like cases [Li($qr + bda$)/Li(st)], the predicted density is $n \approx 0.3 - 1 \times 10^{20}$ ions/cm^3 for 43 eV $< T <$ 46 eV. It is important to note, however, two things about the measured values: (1) the measured values are based on a very preliminary analysis of the data; and (2) the experimental spectrum is time-integrated. Therefore one can expect that the lines emitted from lower ionization stages were observed at an earlier time; that is, when the plasma was at a higher density and somewhat lower temperature.

Figures 2.13(a) through 2.13(j) show the temperature- and density-dependence of intensity ratios for a number of other line combinations. The constraints provided by these other ratios tend to be less good than those described above, but are provided here for completeness. It is worth noting, however, that in no case do the plasma conditions deviate significantly from the values deduced above. That is, the peak temperature reached in the experiment was about 44 eV $\pm$ 4 eV, and this occurred when the density was roughly $10^{-3}\,\rho_{\rm solid}$.

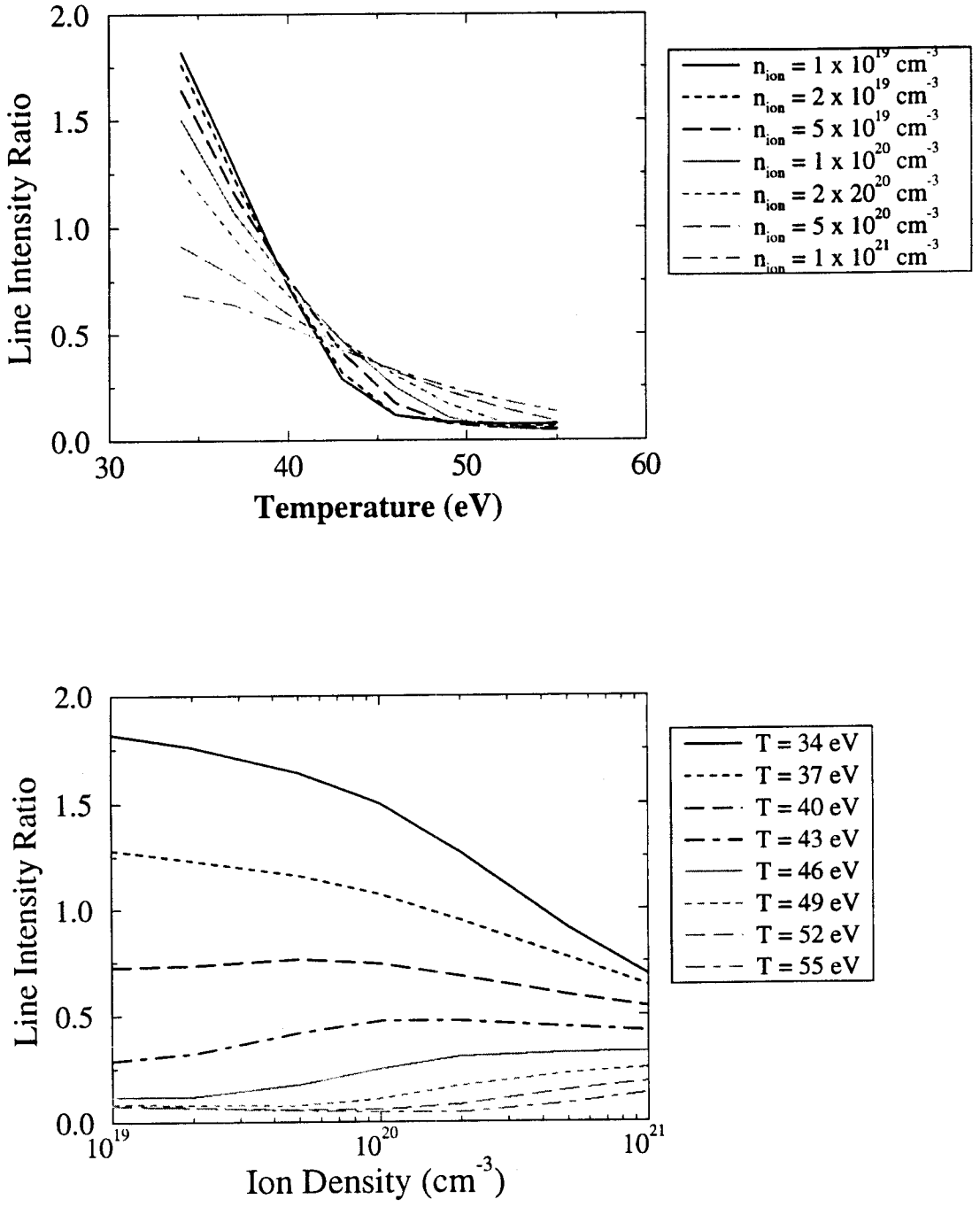

Figure 2.13(a). Temperature and density dependence of line intensity ratio for Li(st)/He$_\alpha$. Line ID's are shown in Fig. 2.4.

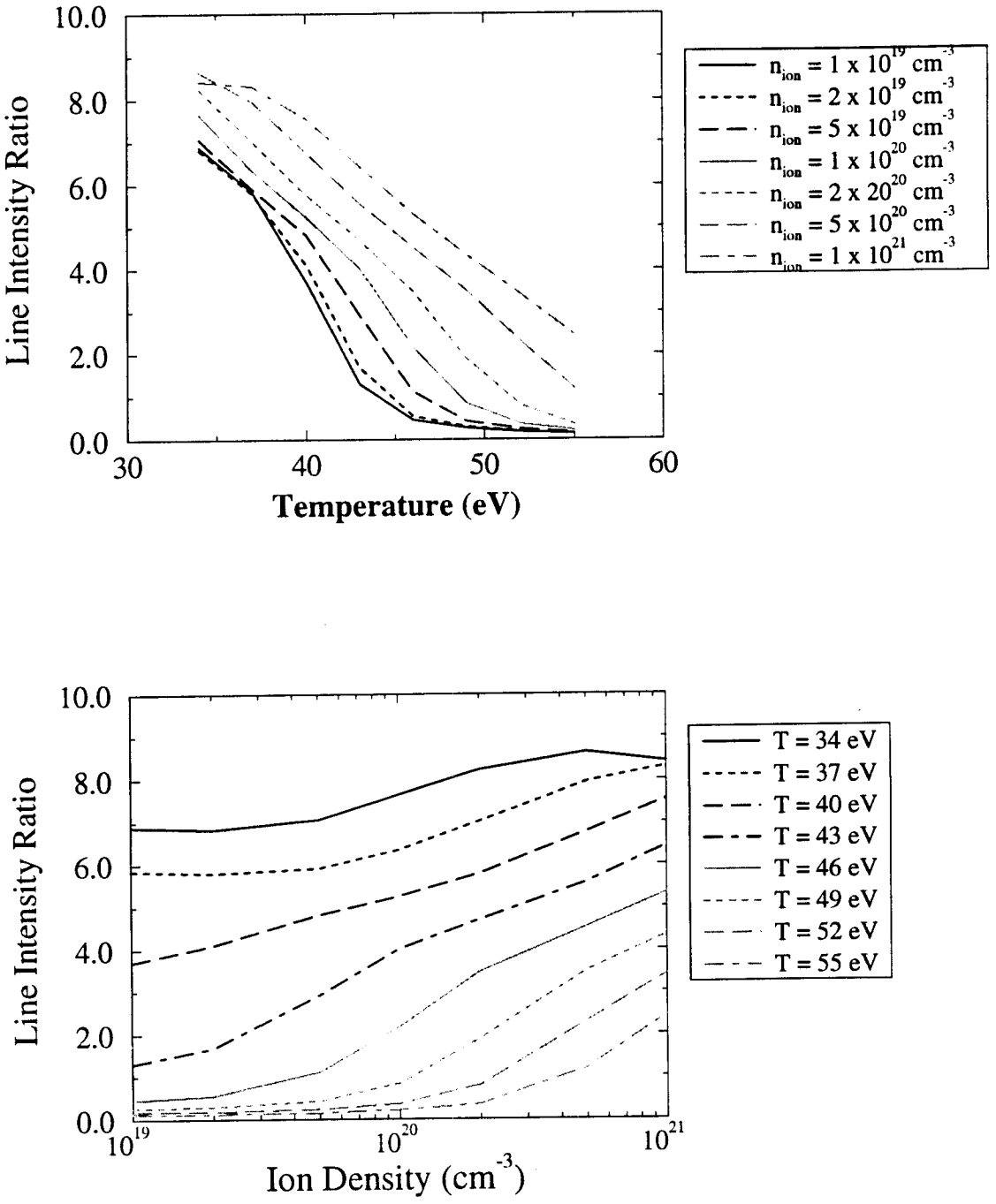

Figure 2.13(b). Temperature and density dependence of line intensity ratio for Li($qr + bda$)/He$_\alpha$. Line ID's are shown in Fig. 2.4.

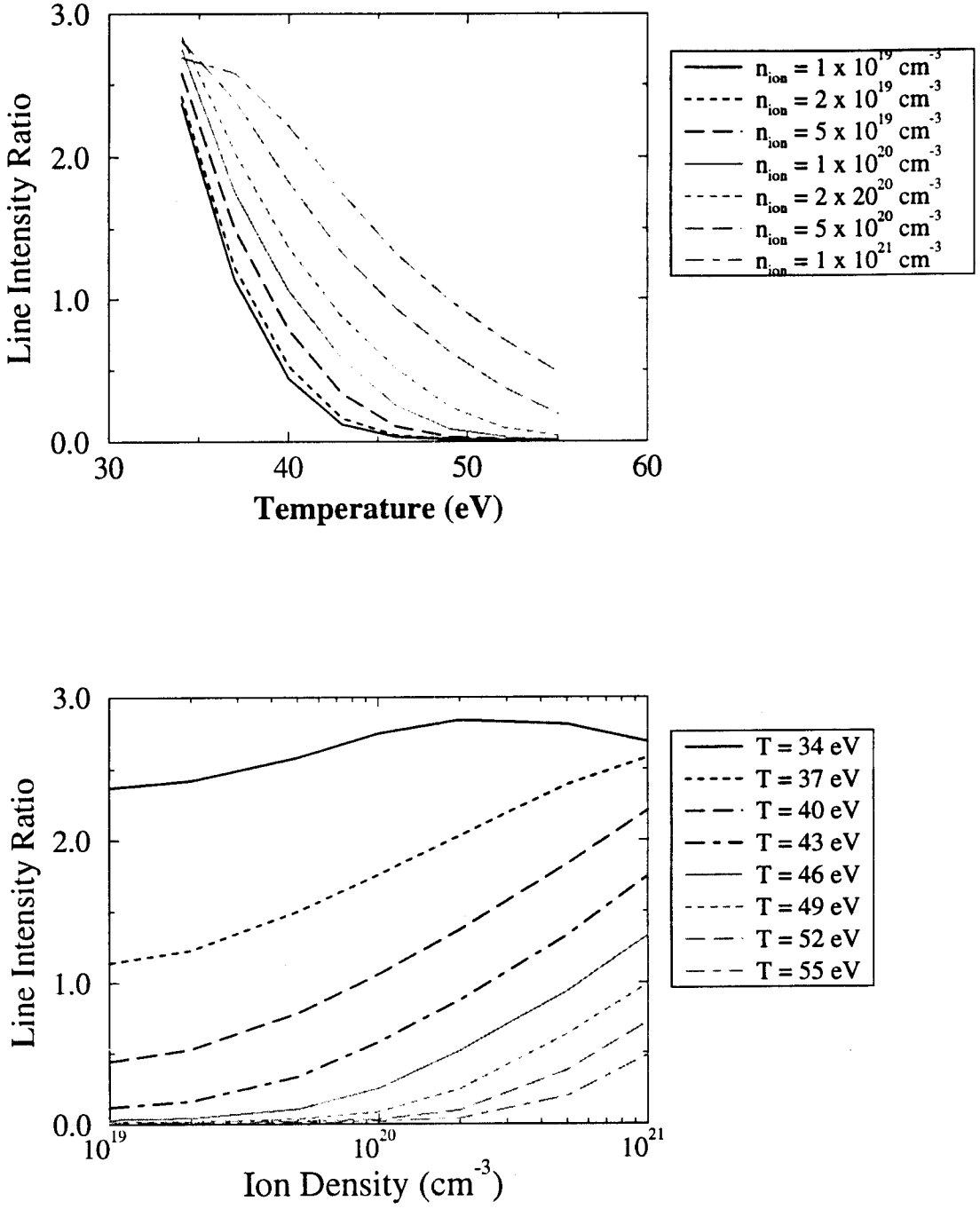

Figure 2.13(c). Temperature and density dependence of line intensity ratio for Li(jk) + Be(jk)*/He$_\alpha$. Line ID's are shown in Fig. 2.4.

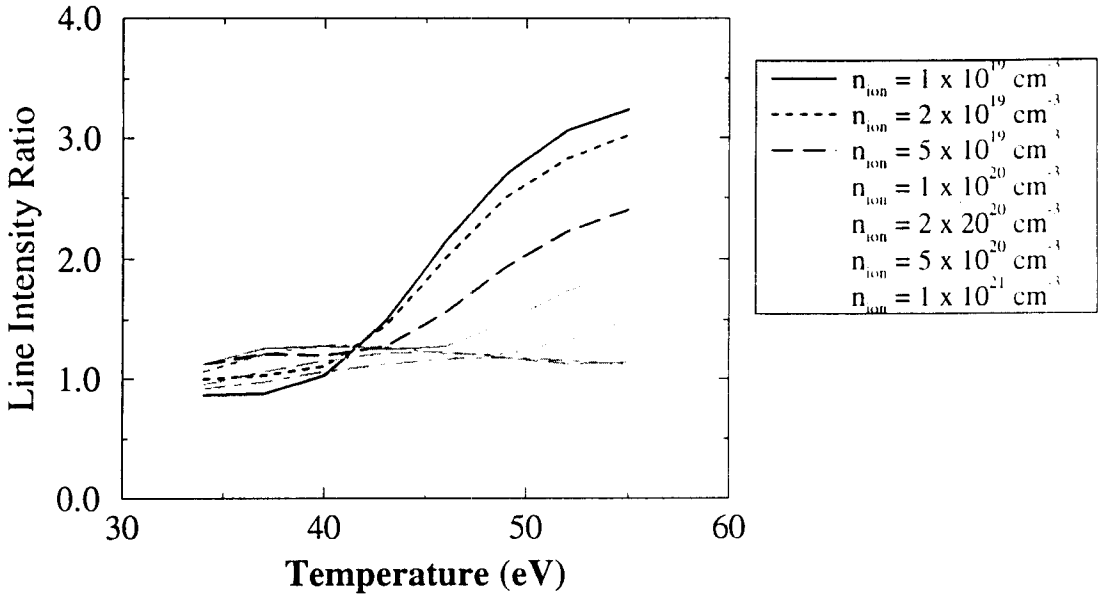

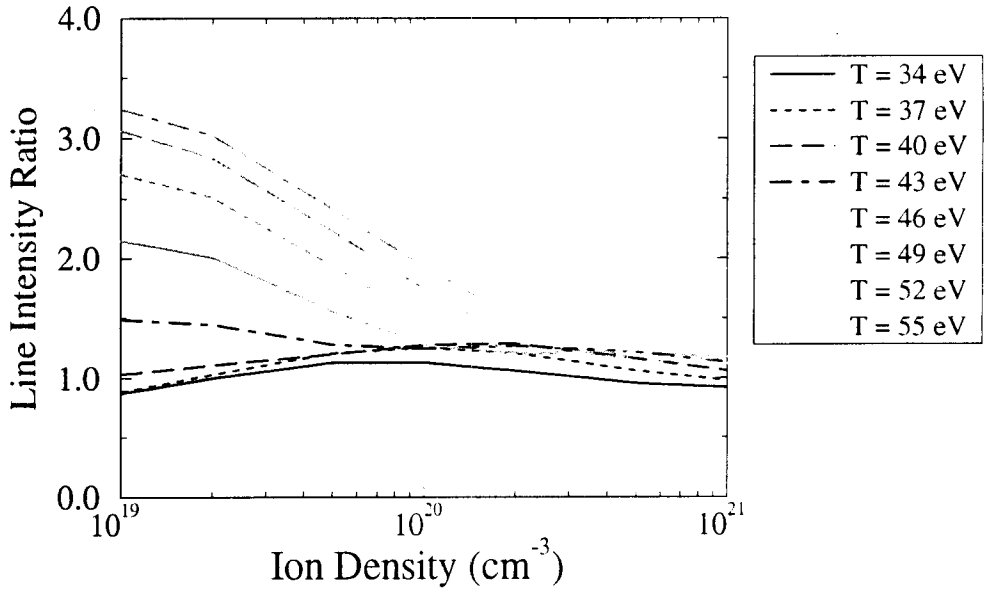

Figure 2.13(d). Temperature and density dependence of line intensity ratio for Li(*bda*)/Li(*qr*). Line ID's are shown in Fig. 2.4.

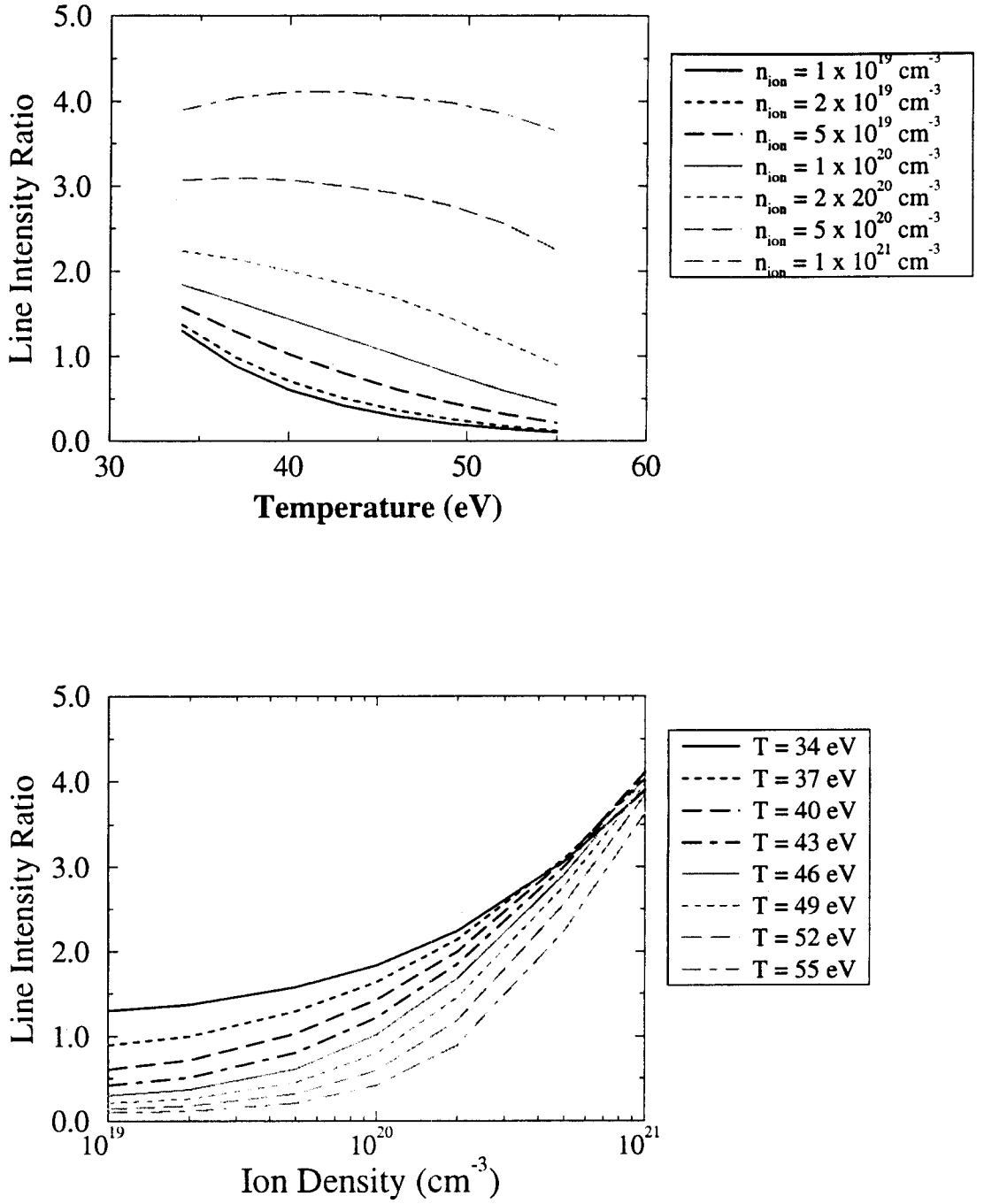

Figure 2.13(e). Temperature and density dependence of line intensity ratio for Li(jk) + Be(jk)*/Li(st). Line ID's are shown in Fig. 2.4.

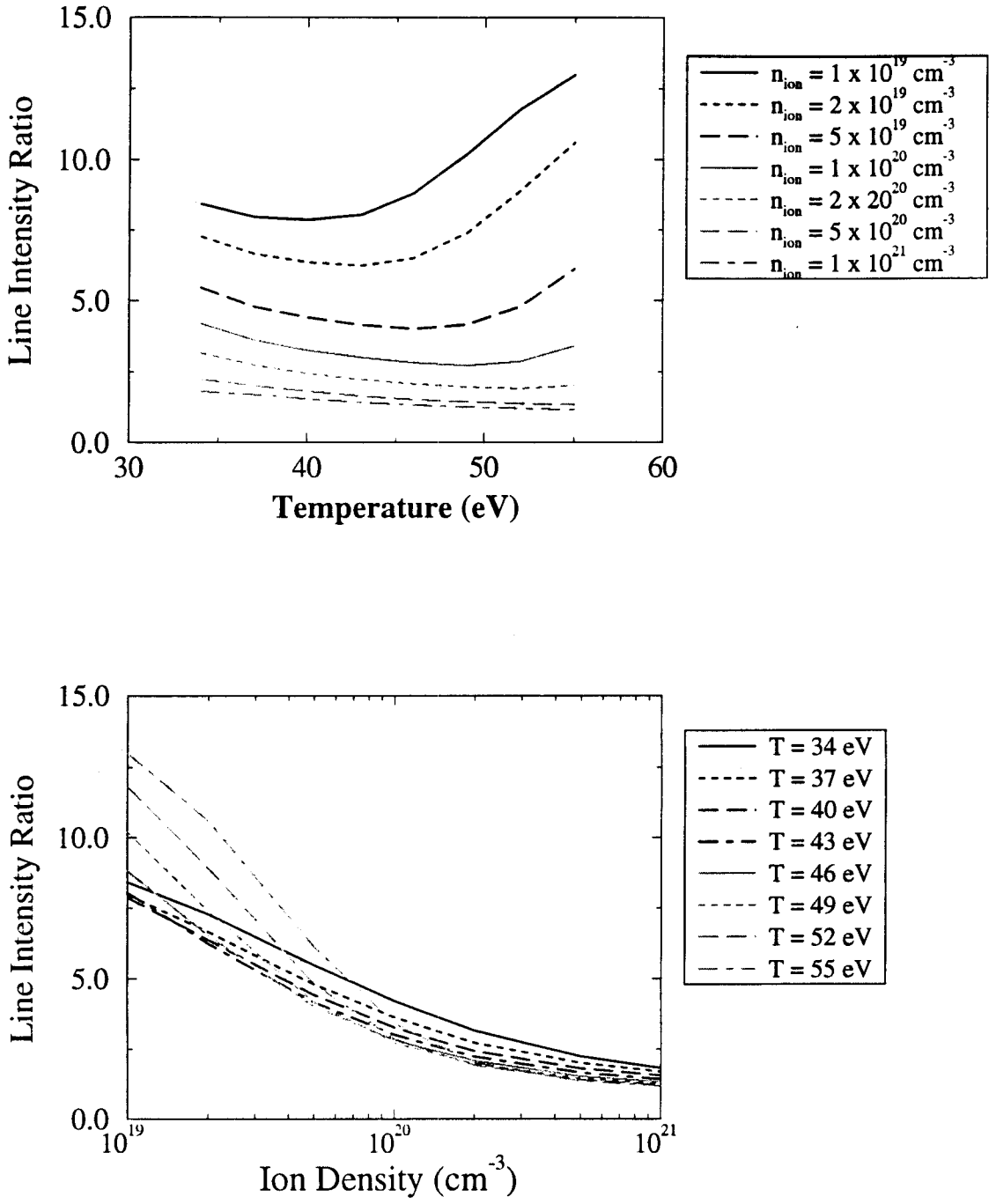

Figure 2.13(f). Temperature and density dependence of line intensity ratio for Li(st)/Li(mn). Line ID's are shown in Fig. 2.4.

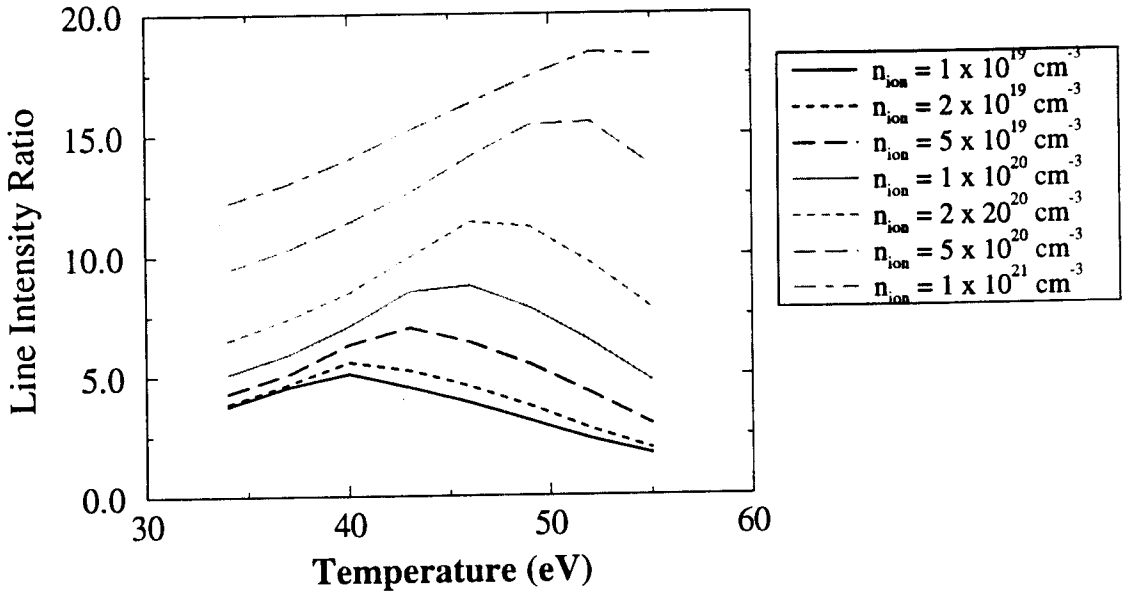

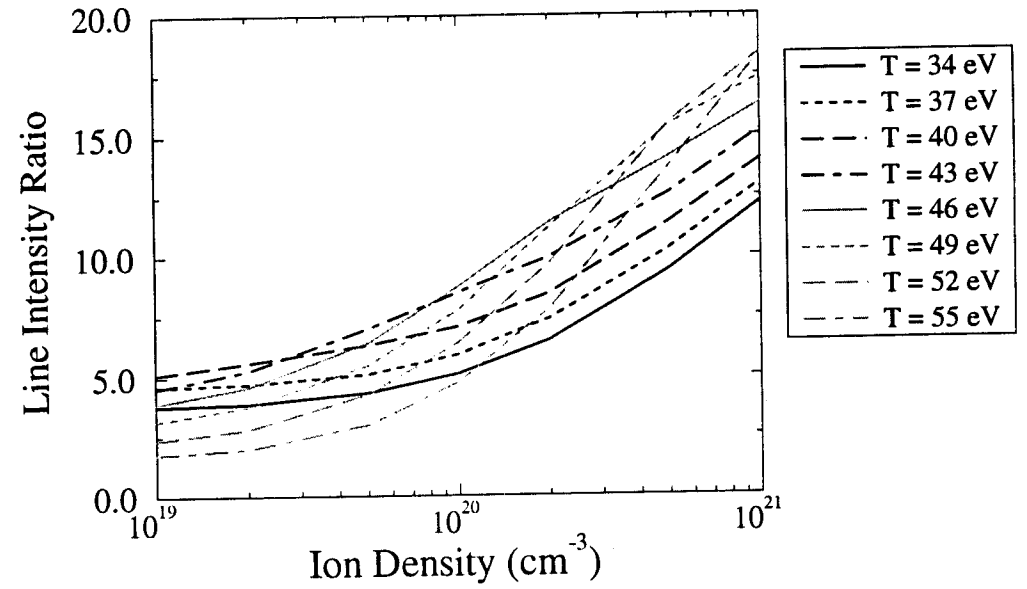

Figure 2.13(g). Temperature and density dependence of line intensity ratio for Li($qr + bda$)/Li(st). Line ID's are shown in Fig. 2.4.

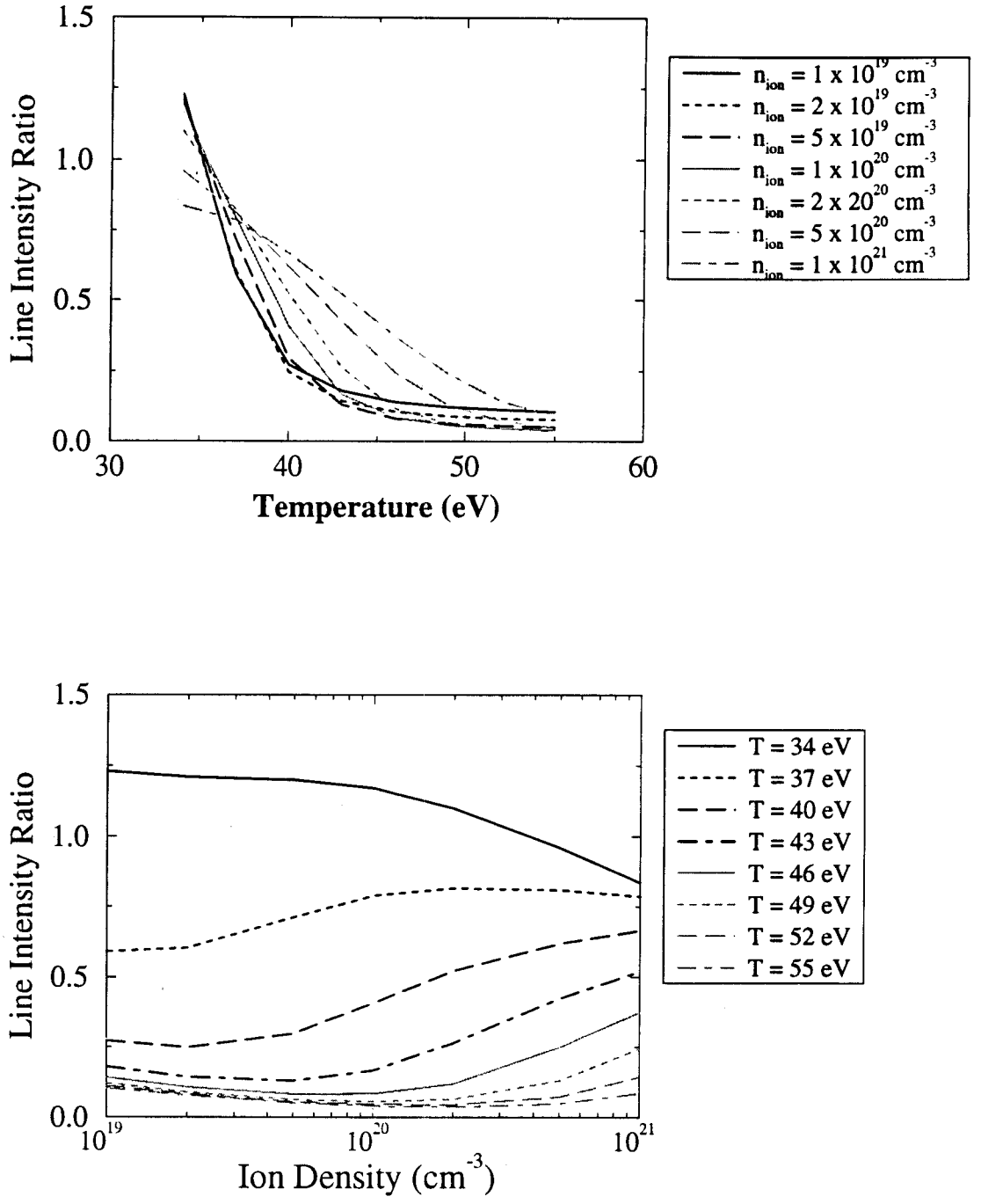

Figure 2.13(h). Temperature and density dependence of line intensity ratio for Be(λ_2)/Li($qr + bda$). Line ID's are shown in Fig. 2.4.

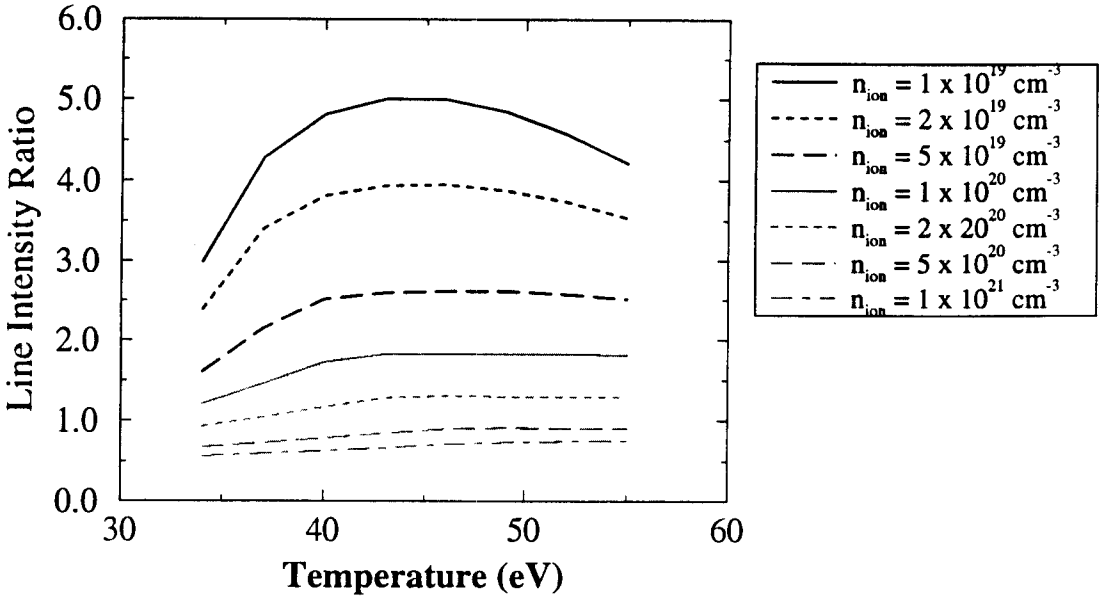

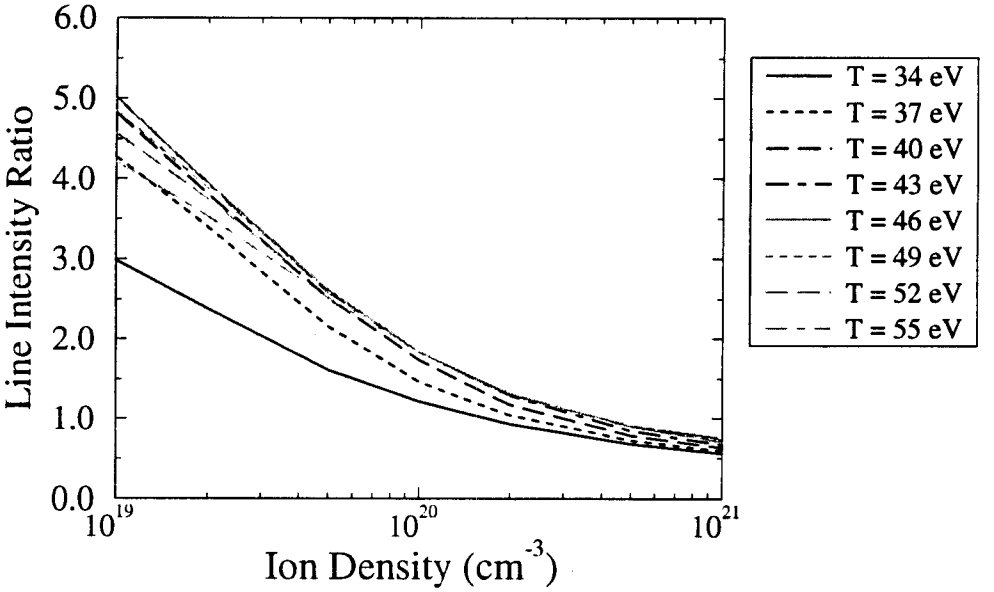

Figure 2.13(i). Temperature and density dependence of line intensity ratio for Be(λ_2)/ Be(λ_1). Line ID's are shown in Fig. 2.4.

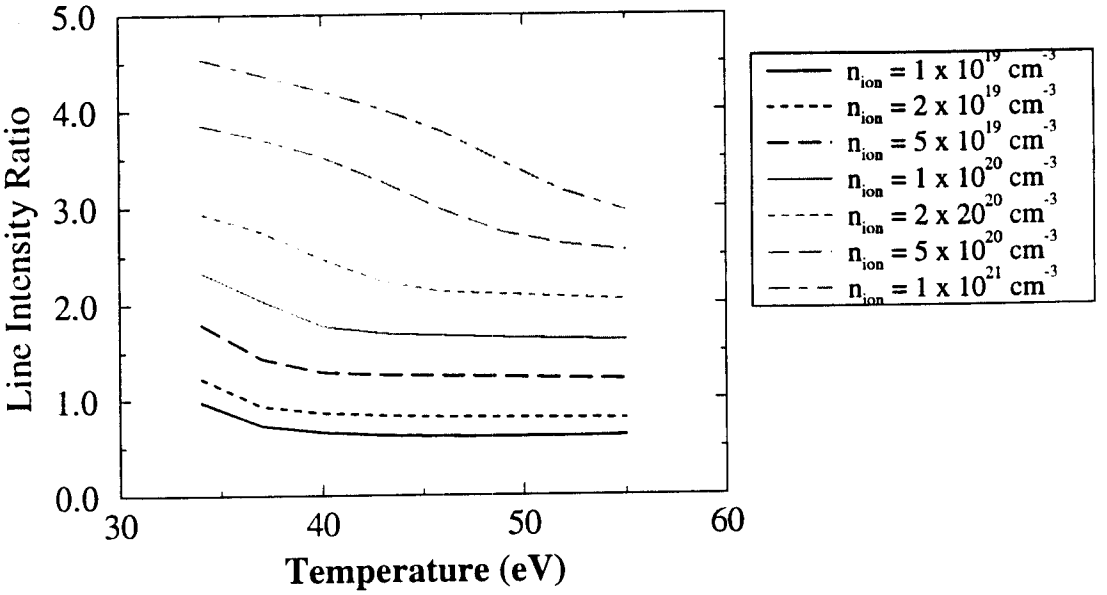

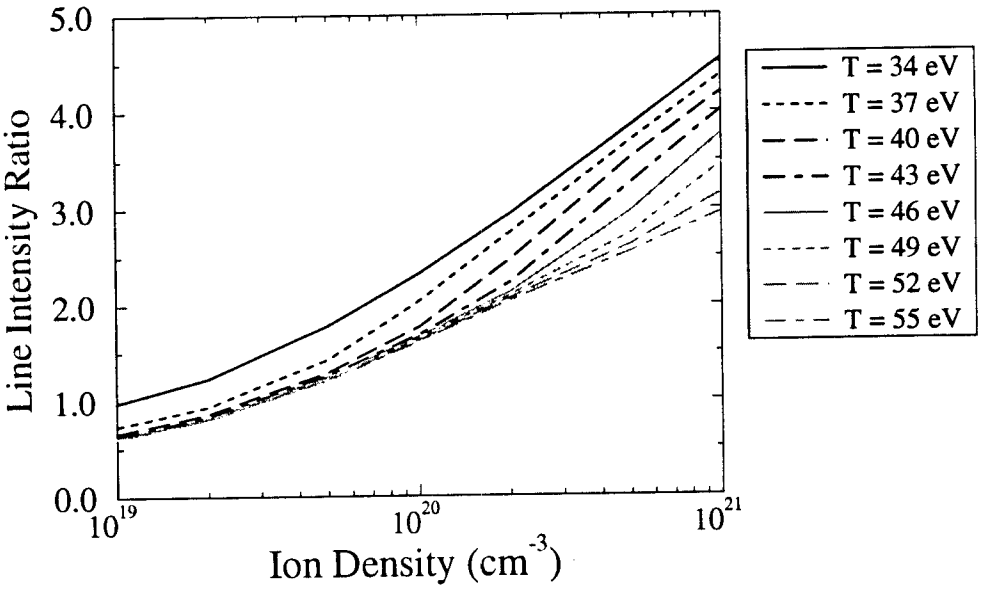

Figure 2.13(j). Temperature and density dependence of line intensity ratio for Be(λ_3)/ Be(λ_2). Line ID's are shown in Fig. 2.4.

Sensitivity Analysis

We have also studied the sensitivity of the plasma conditions deduced from our analysis of K_α line intensity ratios to some uncertainties in the modeling. In particular, we have examined the following potential sources of error:

- multiple ionization cross sections;
- plasma thickness and opacity effects; and
- Li beam energy and power density.

For the first item, we considered 2 extremes in modeling multiple ionization events. In the first case, we set all multiple ionization cross sections to zero. The autoionization levels and $1s2p$ states of He-like Al were thus populated only by transitions in which the ion beam ejects a single K-shell electron (no L-shell electrons). In this case the peak temperature inferred from the intensity ratios of the Li-like to He_α lines was $T \approx 47 - 50$ eV, which is approximately 10% higher than in the analysis described above. In the second case, the calculated ion-impact ionization cross sections were increased as follows: the single (K), double (KL), and triple (KL_2) ionization cross sections were multiplied by factors of 2, 4, and 8, respectively. Larger factors were used for transitions with an increasing number of ionization events because of the larger uncertainties in the calculated cross sections. In this case, the peak temperature deduced from the Li-like to He_α ratios was about $T \approx 40 - 43$ eV, which is $\lesssim 10\%$ lower than in our base case. In both cases the predicted densities are within a factor of a few of $10^{-3}\,\rho_{\rm solid}$.

We also adjusted the thickness of the Al foil in our calculation from $\Delta L = 0$ (optically thin case) to $\Delta L = 4000$ Å. This was done to determine if the predicted plasma conditions are sensitive to the optical path (line of sight) of the observations. For instance, the path length along an angle 45° from the target normal is 1.4 times greater than that which is normal to the surface. So the question arises: are significant errors introduced by utilizing intensities computed along paths normal to the plasma boundary. In these calculations, the inferred plasma properties in the $\Delta L = 4000$ Å case and the 2000 Å case (base case) were virtually identical. By comparison, the optically thin calculations predict a somewhat higher temperature (2–3 eV) because the Li-like satellites are more susceptible to resonant self-absorption effects than the He_α line. Thus, we can conclude that the inferred plasma conditions are not particularly sensitive to the optical path used in the analysis.

Finally, the energy of the Li^{3+} ions and the beam power density were changed in order to assess whether the beam parameters used in our calculations (which assume a monoenergetic beam) could be a significant source of error. A series of calculations was performed in which a 5 MeV Li beam was assumed (down from 9 MeV in the base case). We found the computed line ratios to be almost identical in the two cases. We also performed calculations in which the beam power density was adjusted. Here, as expected, it was found that the K_α flux is proportional to the beam power density, which means line intensities ratios are unaffected. Thus, the predicted plasma conditions inferred from line intensity ratios do not show any significant dependence on uncertainties in the beam parameters.

Summary

From our analysis of Al K_α emission spectra obtained in the plastic sandwich experiments, we conclude that the peak temperature attained (Shot 5881) was approximately $T = 44$ eV ($\pm$ about 10–15%). This temperature was achieved when the density of the expanding target was $\rho \approx 10^{-3}\,\rho_{solid}$ ($\pm$ about a factor of a few). This conclusion is similar to that reached from our previous analysis (MacFarlane and Wang 1993), in which synthetic spectra computed using 1-D LASNEX results were compared with the time-integrated experimental spectra. It is important to note, however, that the plasma conditions obtained from the line ratio method were determined independently of any radiation-hydrodynamic predictions, and depend only on the measured intensities of the He-, Li-, and Be-like K_α satellites. In addition, all of the line intensity ratios examined point to similar plasma conditions. That is, there is no evidence the maximum temperature was signficantly less than 40 eV nor greater than 50 eV. Nonetheless the agreement with our earlier analysis is comforting because the earlier analysis was able to reproduce the observed features from the K_α satellites from the lower ionization stages of Al as well. Thus, these two types of analysis provide complementary information, and a consistent picture for the plasma conditions.

The sensitivity of our results to uncertainties in our CRE and atomic physics models was also addressed. It was seen that the greatest source of error in our analysis is the uncertainties associated with the calculated multiple ionization cross sections, which can introduce errors of up to about 10% in the plasma temperature. Possible errors associated with opacity effects or assumptions of the beam energy were found to be even smaller. Additional constraints on plasma conditions could be obtained using

multicomponent tracers (e.g., Mg and Al), or by measuring both emission and absorption spectra simultaneously.

To conclude, it is felt that analyzing K_α line intensity ratios offers an excellent opportunity for diagnosing plasma conditions in intense light ion beam experiments. In principal, this method could be applied to targets containing multiple tracers to determine plasma conditions at separate points within a target, thus providing some spatial resolution and information about energy flow in the target. Because the K_α lines are emitted at x-ray wavelengths, they can be used to probe conditions of the interior of a target. It is advantageous to examine lines from relatively high ionization stages (He-like, Li-like, and perhaps Be-like) of the tracer for determining the target plasma temperature and density because the strongest transitions are more easily resolved. It has also been shown (see Section 3) that instrumental broadening is the dominant source of broadening for the K_α satellites in the PBFA-II experiments. Thus, this technique of using line intensity ratios can benefit significantly from improvements in the spectral resolution (as well as time resolution). It is recommended that this technique be exploited in future PBFA-II beam-plasma interaction experiments to study basic physics issues relevant to ICF targets.

2.E. Effects of Dielectronic Recombination on K_α Emission Spectra

In light-ion beam heated plasmas, in addition to inner-shell ion-impact ionization, K_α x-ray line emission can also be produced by dielectronic recombination involving excitation of an electron out of the $1s$ shell; for example:

$$1s^2 2s^2 2p^2 + \varepsilon(l \pm 1) \rightarrow 1s^1 2s^2 2p^3 nl \rightarrow 1s^2 2s^2 2p^2 nl. \tag{2.1}$$

Dielectronic recombination may be thought of as a resonance in a (radiationless) inelastic scattering process in which the incident free electron loses 100% of its kinetic energy, and thereby becomes captured. For aluminum ions, to induce dielectronic recombination processes of the type indicated in Eq. (2.1), there must be free electrons with kinetic energies $\varepsilon > 1000$ eV in the plasma. For the plasma conditions of current interest, ($N_e \sim 10^{20}$ cm^{-3}, $T_e \leq 50$ eV), the fraction of electrons with these high energies is very small. In our previous numerical analyses of K_α satellite line emission spectra produced in PBFA II experiments, ion-impact ionization by beam ions was assumed to be the dominant populating mechanism for the autoionization levels. Dielectronic recombination was assumed to have a negligible effect. However, the question arises: at

what temperature does dielectronic recombination begin to influence the K_α emission spectrum.

To check the effects of dielectronic recombination on K_α satellite emission spectra, we compare the populating rates of autoionizing levels with K-shell vacancies due to the two different processes: ion-impact ionization and dielectronic recombination. These processes are illustrated in Fig. 2.14 for the fluorescing transition:

$$1s^1 2s^2 2p^3 \rightarrow 1s^2 2s^2 2p^2 \,.$$

The rates at which the $1s^1 2s^2 2p^3$ level is populated by inner-shell ion beam impact ionization:

$$I_i(1/s) = N_1 \times 6.242 \times \frac{P_{\rm beam}({\rm TW/cm^2})}{E_{\rm beam}({\rm MeV})} \times \sigma({\rm barn})\,, \tag{2.2}$$

where N_1 is particle density of target ions in the level 1 (in $\rm cm^{-3}$), $P_{\rm beam}$ is the power density of incident ion beam, $E_{\rm beam}$ is the energy of the ion beam, and σ is inner-shell ion impact ionization cross section. The rate for dielectronic recombination is:

$$\alpha_d(1/{\rm s}) = N_3 N_e \times 1.656 \times 10^{-22} \frac{A_a^{4-3}}{T_e({\rm eV})} \times \frac{g_4}{g_3} \exp(-\Delta E_{43}/Te)\,, \tag{2.3}$$

where N_3 is particle density of ions in the level 3 (in $\rm cm^{-3}$), N_e is electron density, T_e is electron temperature, A_a^{4-3} is autoionization rate of level 4, and g_3 and g_4 are the statistical weights of level 3 and 4, respectively. Eq. (2.3) is obtained from the inverse (autoionization) process by means of the principle of detailed balance. This expression holds whether or not the ion populations correspond to equilibrium conditions, provided that the free electrons have a Maxwell-Boltzmann velocity distribution.

If $\alpha_d \ll I_i$, the populations of autoionizing levels are determined by inner-shell ion-impact ionization processes, and the effects of dielectronic recombination on K_α emission line spectra can be ignored. At sufficiently high temperatures, however, dielectronic recombination will become important. Below we considered the following dielectronic recombination transitions which result in K-shell vacancies:

- For Li-like Al ions

$$1s^2 + e^- \rightarrow 1s^1 2s^1 2p^1,$$
$$1s^2 + e^- \rightarrow 1s^1 2p^2,$$
$$1s^2 + e^- \rightarrow 1s^1 2p^1 3l^1 (l = s, p, d)\,.$$

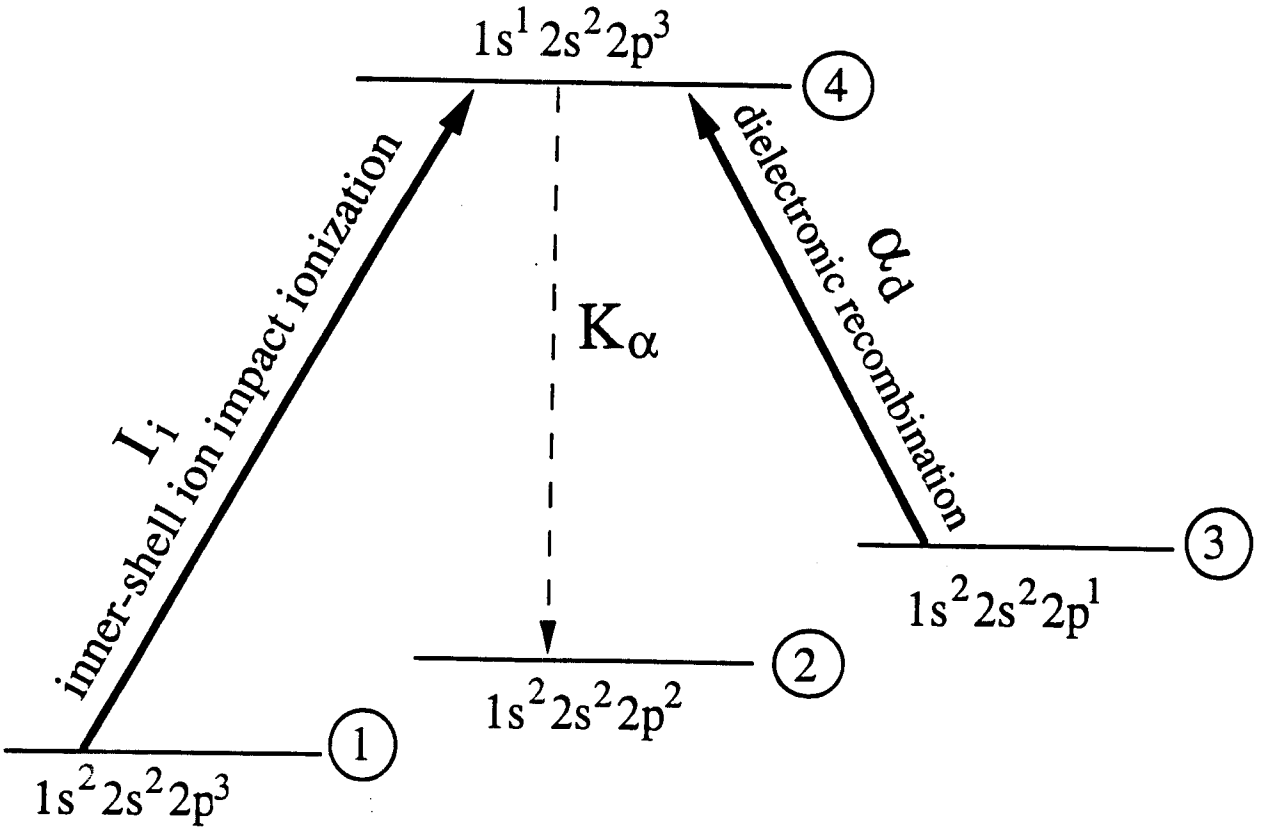

Figure 2.14. Simplified energy level diagram showing competing processes of dielectronic recombination and ion-impact ionization in populating the $1s^1 2s^2 2p^3$ autoionization level.

- For Be-like Al ions

$$1s^2 2s^1 + e^- \rightarrow 1s^1 2s^2 2p^1,$$
$$1s^2 2s^1 + e^- \rightarrow 1s^1 2s^1 2p^2,$$
$$1s^2 2p^1 + e^- \rightarrow 1s^1 2p^3,$$
$$1s^2 2s^1 + e^- \rightarrow 1s^1 2s^1 2p^1 3l^1 (l = s, p, d).$$

- For B-like Al ions

$$1s^2 2s^2 + e^- \rightarrow 1s^1 2s^2 2p^2,$$
$$1s^2 2s^1 2p^1 + e^- \rightarrow 1s^1 2s^1 2p^3,$$
$$1s^2 2p^2 + e^- \rightarrow 1s^1 2p^4,$$
$$1s^2 2s^2 + e^- \rightarrow 1s^1 2s^2 2p^1 3l^1 (l = s, p, d).$$

To compute dielectronic recombination rates, one must first calculate the related autoionization transition probability A_a. We have calculated autoionization probabilities from the first-order perturbation theory expression (Fano 1961):

$$A_a(\gamma_i, 1s, \epsilon l_4, L'S'J' \rightarrow \gamma_f, n_1 l_1, n_2 l_2, LSJ) = 2\pi \sum | < i|1/r_{12}|f > |^2 \qquad (2.4)$$

and

$$< i|1/r_{12}|f >= \sum_k x_k R^k(1s, \epsilon l_4; n_1 l_1, n_2 l_2|r), \qquad (2.5)$$

where the A_a is autoionization rate in atomic units, the transition $(1s, \epsilon l) \rightarrow (n_1 l_1, n_2 l_2)$ refers to the exchange of holes between the initial and final states, x_k is a coefficient related to the angular momentum coupling and can be expressed with $3j$ and $6j$ symbols, and the $R^k(r)$ are radial integrals defined as follows:

$$R^k(l_1 l_2 l_3 l_4) = \int_0^\infty \int_0^\infty \frac{\gamma_<^k}{\gamma_>^{k+1}} P^*_{n_1 l_1}(\gamma_i) P^*_{n_2 l_2}(\gamma_j) P_{n_3 l_3}(\gamma_i) P_{\epsilon l_4}(\gamma_j) dr_i dr_j . \qquad (2.6)$$

The radial wavefunctions $P_{nl}(r)$ are calculated by solving the Hartree-Fock equations. The continuum wavefunction $P_{\epsilon l}(r)$ for a free electron of kinetic energy $\epsilon = \Delta E_{34}$ is normalized to $\delta(\epsilon - \epsilon')$. This continuum function is obtained from solving a radial Schrödinger equation by using the HX method (Cowan 1981).

In our calculations, atomic structure data and autoionization rates are calculated using an intermediate coupling scheme with all fine-structure components of the $2p - 1s$

transitions taken into account. Free electrons are assumed to have a Maxwellian distribution with density $N_e = 8 \times 10^{20}$ cm^{-3}, which is based on a CRE calculation for an Al plasma at $T = 45$ eV and $N_{\rm ion} = 10^{20}$ cm^{-3}.

Figure 2.15 shows the populating rates of various autoionizing levels due to dielectronic recombination for Li-like Al ions. Also shown in the figure are the corresponding ion-impact ionization rates by a 3 TW/cm^2, 9 MeV Li beam. In the figure, the ion-impact ionization rates are marked with two horizontal lines, which indicate the variation of ionization cross sections with the different target states. It can be seen from the figure that dielectronic recombination rates are sensitive to the final autoionization states. For example, the dielectronic recombination rate for $1s^2 + e^- \rightarrow 1s^1 2p^1 3d^1$ is about two orders of magnitude smaller than that for the $1s^2 + e^- \rightarrow 1s^1 2s^1 2p^1$ transition at $T = 100$ eV. This is because higher velocity electrons are required to induce dielectronic recombination for $1s^2 + e^- \rightarrow 1s^1 2p^1 3d^1$, and the number of high velocity electrons decreases very rapidly for low temperature plasmas. For the same target state, dielectronic recombination rates are smaller for higher energy recombined autoionizing state. In other words, for K_α emissions produced by the dielectronic recombination process, the intensity of emissions from excited states with M-shell spectator electrons will be weaker than those from lower states such as $1s^1 2s^1 2p^1$. Similarly, for K_α emissions induced by ion-impact ionization, the K_α lines from transitions involving excited configuration states with M-shell spectator electrons are usually weaker than those from ground configuration states because of the lower populations of excited configuration states.

Note that for relatively low temperature aluminum plasmas ($T_e \lesssim 50$ eV), the dielectronic recombination rate coefficients are much smaller than the ion impact ionization rate coefficients. Thus the effects of dielectronic recombination on the K_α satellite emission spectra should be unimportant. (Note the rates are *per ion*, so that N_1 and N_3 in Eqs. (2.2) and (2.3) are not actually computed). The dielectronic recombination rate increases very rapidly as the plasma temperature increases. Fig. 2.15 shows that dielectronic recombination rates become competitive with ion impact ionization rates when $T_e \gtrsim 70$ eV. In fact, at $T_e \gtrsim 130$ eV dielectronic recombination becomes the dominant process in producing K-shell vacancies. Similar results are obtained for Be- and B-like ions, which are shown in Figs. 2.16 and 2.17.

This study on dielectronic recombination effects suggests that for the plasma conditions attained in the PBFA-II experiments to date, the effects of dielectronic

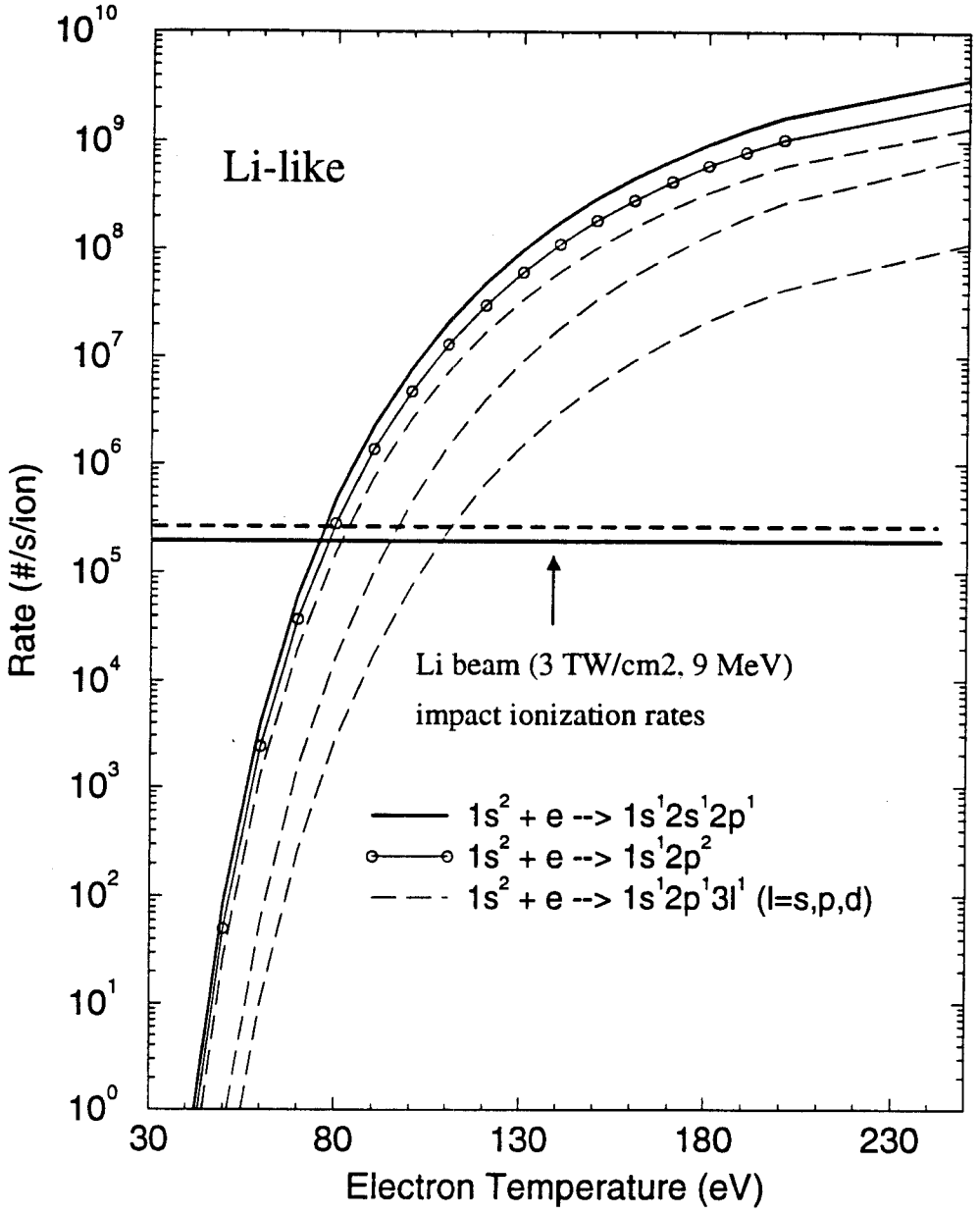

Figure 2.15. Temperature dependence of dielectronic recombination rate coefficients for various transitions resulting in Li-like Al with a K-shell vacancy. The horizontal lines represent ion-impact ionization rate coefficients for transitions populating the same autoionizing levels. Note that ion-impact ionization dominates for plasma temperatures $\lesssim 60$ eV.

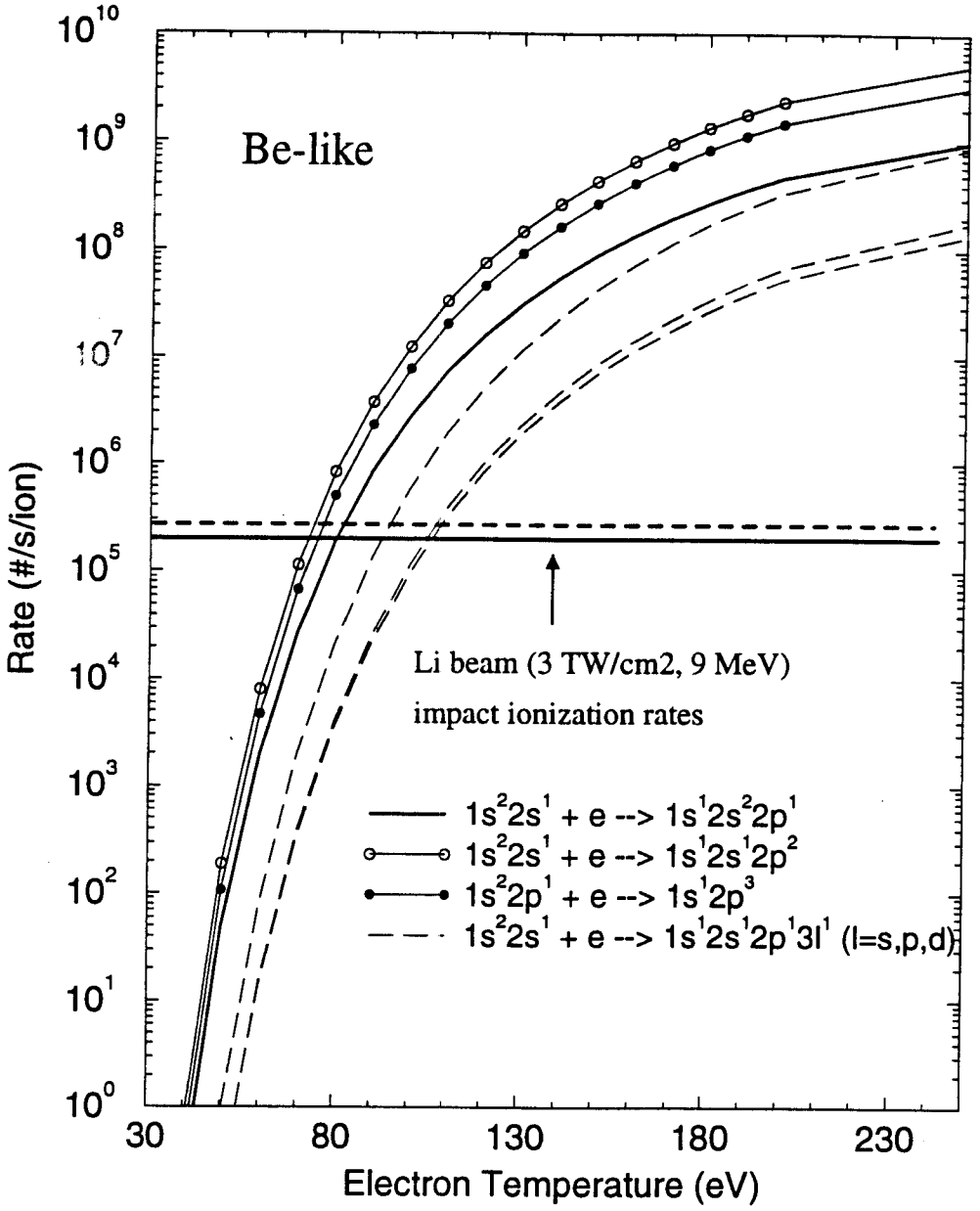

Figure 2.16. Temperature dependence of dielectronic recombination rate coefficients for various transitions resulting in Be-like Al with a K-shell vacancy. The horizontal lines represent ion-impact ionization rate coefficients for transitions populating the same autoionizing levels. Note that ion-impact ionization dominates for plasma temperatures $\lesssim$ 60 eV.

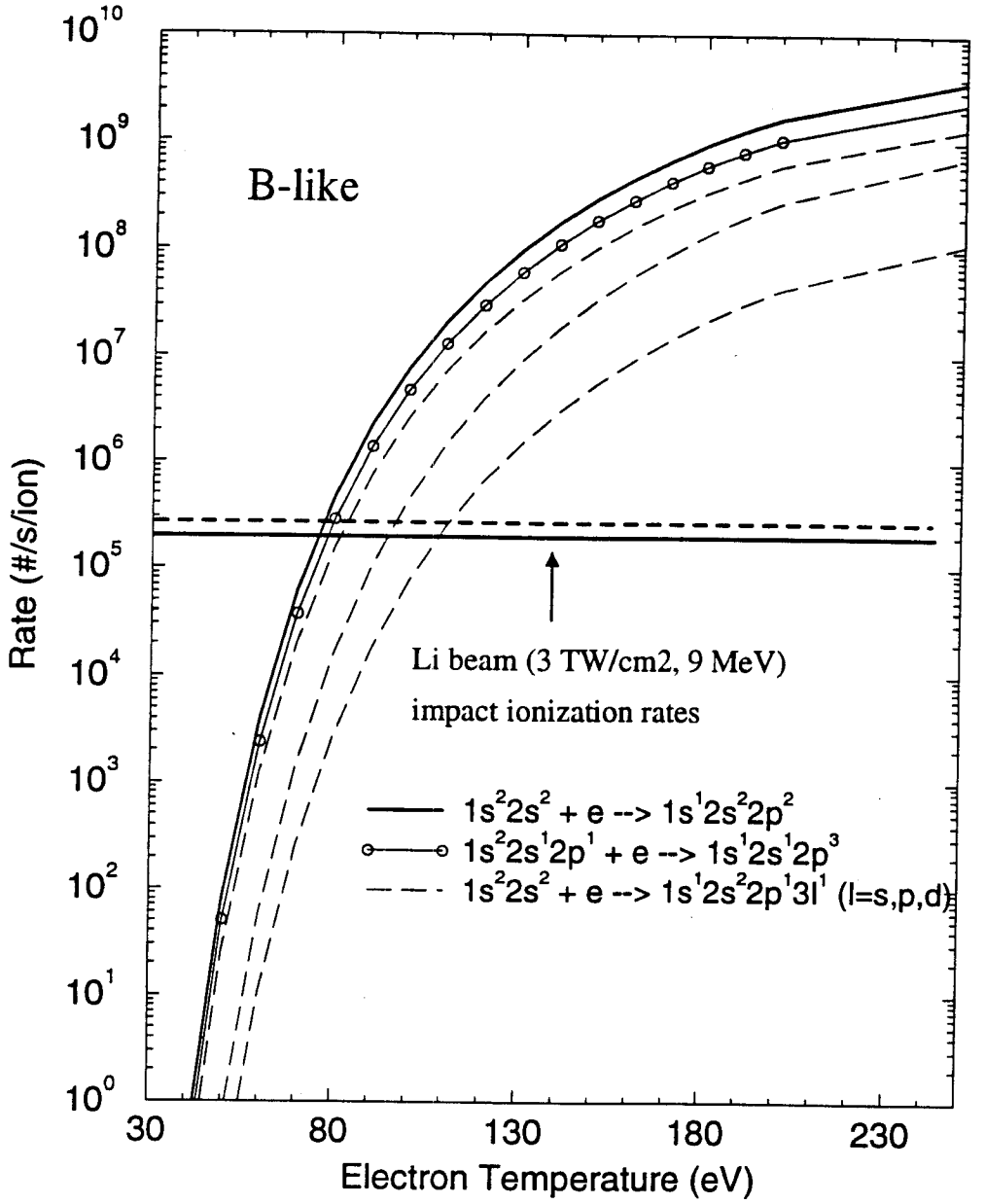

Figure 2.17. Temperature dependence of dielectronic recombination rate coefficients for various transitions resulting in B-like Al with a K-shell vacancy. The horizontal lines represent ion-impact ionization rate coefficients for transitions populating the same autoionizing levels. Note that ion-impact ionization dominates for plasma temperatures $\lesssim$ 60 eV.

recombination on measured K_α satellite emission spectra are unimportant. However, in future experiments dielectronic recombination processes could significantly impact K_α spectra measurements when higher plasma temperatures are attained.

2.F. Calculation of Aluminum Thermal Spectrum and Radiation Flux

To assist in the analysis of radiation-hydrodynamics simulations of the K_α plastic sandwich experiments, we have calculated the total radiation (thermal) flux emitted from a thin Al plasma using detailed radiation and atomic physics models. It is important to accurately model radiation transport and losses in the target plasma because it plays a critical role in the overall energetics of the problem. This is evidenced by the fact that the maximum temperature in the Al plasma predicted by the 1-D LASNEX simulations of these experiments changes dramatically when the Al opacities are adjusted (Dukart 1993). Currently, there is a discrepancy between the peak temperatures deduced from the K_α emission spectra ($T \approx 44$ eV) and those predicted by the radiation-hydrodynamics simulations using measured Li beam parameters ($T \approx 27$ eV). That is, using the measured beam power density, the temperatures predicted by the LASNEX simulations are substantially lower than those deduced from the analysis of K_α emission spectra.

There are several possible explanations for the low LASNEX temperatures, including: (1) the stopping powers in the Al and/or Au layers are underestimated; (2) radiation losses out of the Al layer are overestimated; (3) the rate at which radiative energy is transported from the Au layer and absorbed by the Al layer is underestimated; and (4) multidimensional effects not accounted for in the 1-D simulations lead to large errors. The purpose of the calculations described below address item (2).

Plasma conditions of the type described here (i.e., moderate densities with $\tau_\nu \ll 1$ for the continuum and $\tau_\nu \gg 1$ for lines, where τ_ν is the frequency-dependent optical depth) present several challenges in regards to modelling. First, radiation diffusion models may be inaccurate because they are based on the assumption that the photon mean free paths are small compared to the characteristic plasma dimensions. Second, the radiation transport equation should be solved at a large number of frequency points to account for all of the structure in the spectra; that is, each of the large number of lines needs to be resolved on the computational frequency grid. Because of computational considerations, radiative transfer models within radiation-hydrodynamics codes often utilize approximations which can lead to significant inaccuracies in the computed radiation flux. For instance, in our analysis of ICF reactor target chamber

plasmas (which have lower densities ($\sim 10^{16} - 10^{17}$ cm^{-3}), but similar optical depth properties to the plasmas discussed here), it was found (MacFarlane and Wang 1991) that the multigroup radiation diffusion model used in our target chamber radiation-hydrodynamics code predicted fluxes which were $\sim 10^1 - 10^2$ higher than those predicted in our CRE calculations.

Here, we consider a planar Al plasma with the following conditions: $T = 30$ eV, $n = 10^{20}$ ions/cm^3 ($\rho = 4.5 \times 10^{-3}$ g/cm^3), and $\Delta L = 120\,\mu$m. The thickness corresponds to a 2000 Å-thick foil which has expanded 600 times. Non-LTE atomic level populations were computed using a CRE model which includes photoexcitation effects. (The deviation from LTE, however, is not especially significant.) Radiation is transported using a multiangle, multifrequency transport model. A total of more than 200 energy levels were included in the atomic model for Al.

Figures 2.18 and 2.19 show the frequency-dependent optical depth and emission flux at the plasma boundary. The optical depth is computed along a path normal to the boundary. Note that the Al is *not* optically thick at all frequencies, and therefore one should not expect the emission spectrum to resemble anything like a blackbody continuum in spite of the fact that the atomic level populations can be close to LTE. Between 20 and 200 eV, the mean free paths of *continuum* photons are typically $10^1 - 10^2$ larger than the plasma dimensions (that is, $\tau_\nu \sim 10^{-2} - 10^{-1}$). On the other hand, many of the lines are optically thick ($\tau_\nu \gg 1$). Thus, one can expect that the emission flux in the line cores should be near their Planckian values.

These points can be easily understood by examining the integral form of the transfer equation (see, e.g., Mihalas 1978):

$$I_\nu = \int_0^{T_\nu} S_\nu(t) e^{-t}\, dt\,, \tag{2.7}$$

where I_ν is the specific intensity at the plasma boundary, S_ν is the source function ($\equiv \eta_\nu/\chi_\nu$), and T_ν is the total optical depth. For simplicity, Eq. (2.7) has been written for a photon travelling along a path normal to the plasma boundary. When the plasma is in LTE, $S_\nu = B_\nu$ ($\equiv$ Planck function). Then, for an isothermal plasma of temperature T, we have:

$$\begin{aligned} I_\nu &= B_\nu(T) \int_0^{T_\nu} e^{-t}\, dt \\ &= B_\nu(T)\,[1 - e^{-T_\nu}]\,. \end{aligned}$$

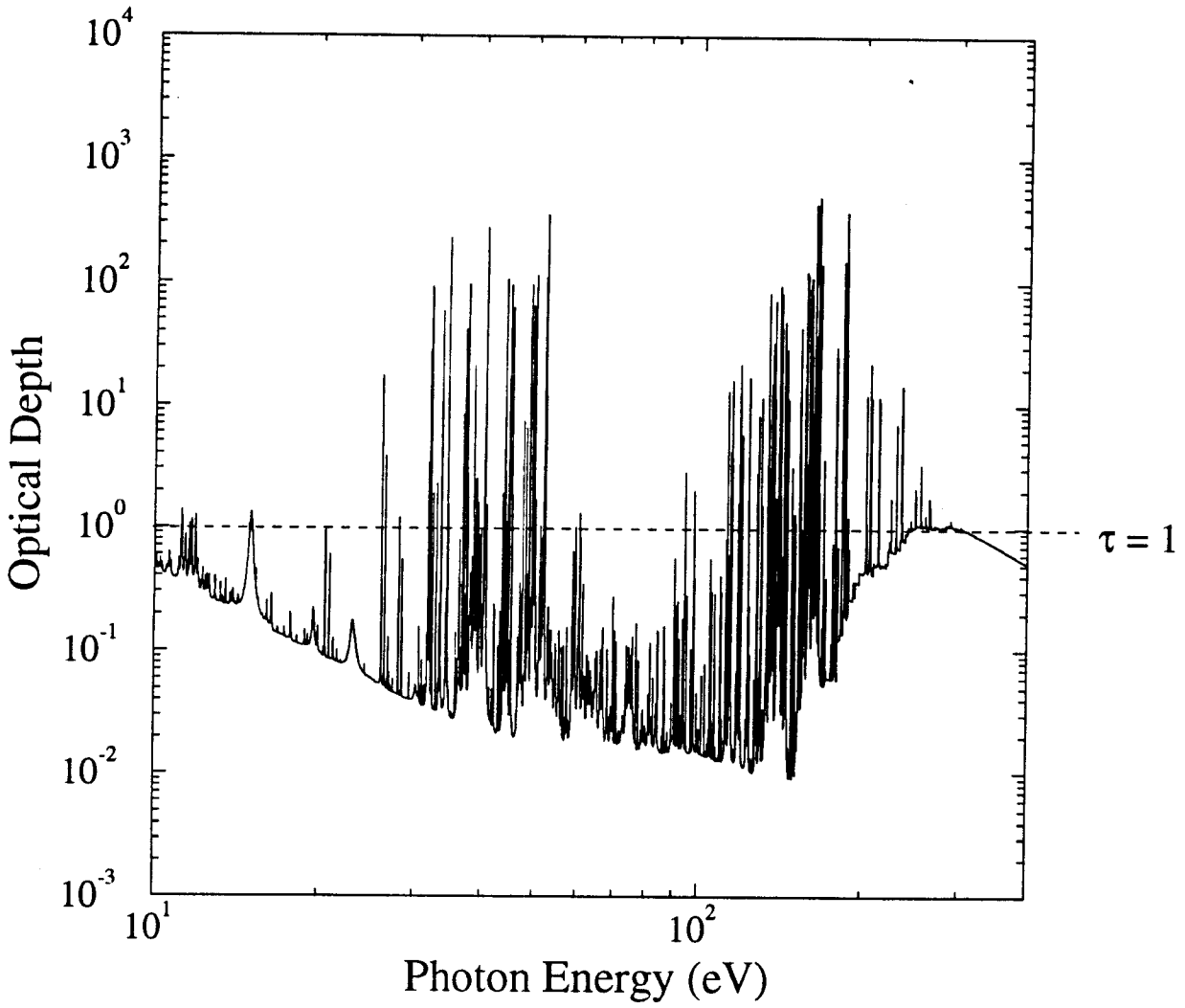

Figure 2.18. Calculated frequency-dependent optical depth for an Al plasma at $T = 30$ eV, $n = 10^{20}$ ions/cm^3, and $L = 120\,\mu$m.

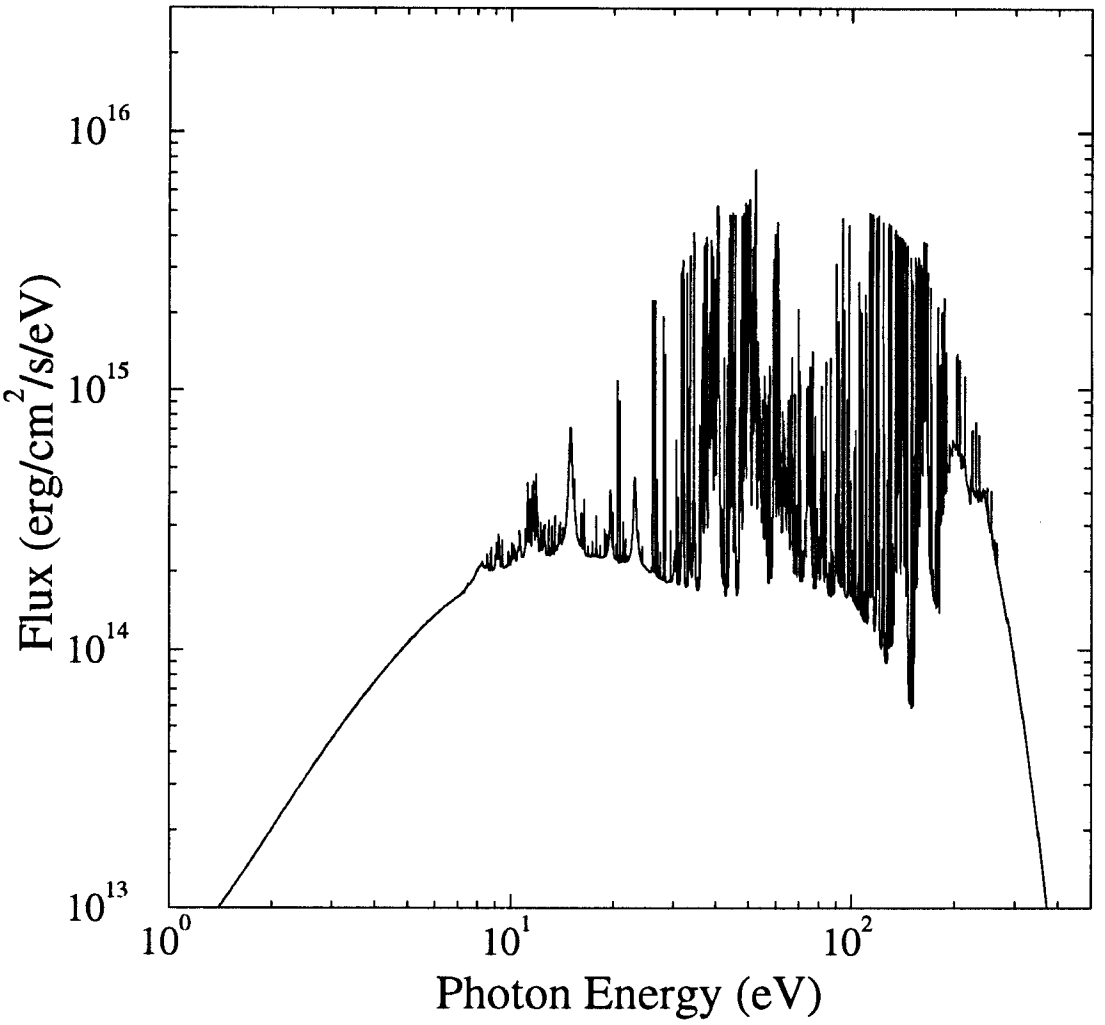

Figure 2.19. Calculated frequency-dependent flux emitted by an Al plasma at $T = 30$ eV, $n = 10^{20}$ ions/cm^3, and $L = 120\,\mu$m.

At frequencies where the plasma is optically thin ($T_\nu \ll 1$), the intensity is simply proportional to the plasma thickness. When $T_\nu \gg 1$, the intensity approaches the Planck value.

This effect is clearly seen in Fig. 2.19, where $\mathcal{F}_\nu \ll B_\nu$ in regions where the optical depth is low and $\mathcal{F}_\nu \approx B_\nu$ in the cores of optically thick lines.

The total (frequency-integrated) flux is 1.5×10^{17} erg/cm^2/s. This corresponds to a radiation temperature of

$$T_R = \left(\frac{\text{Flux}}{\sigma_{SB}} \right)^{1/4} = 19.5\,\text{eV}\,.$$

This corresponds to a flux which is a factor of 5.7 lower than the blackbody value. By comparison, the value predicted by the model used in the LASNEX simulations is approximately $T_R \approx 25$ eV (Bailey 1993), which corresponds to a flux which is about 2.7 greater than that obtained from our CRE calculations.

The above results *suggest* the radiation losses in the Al layer are being overestimated in the LASNEX simulations. We say this because the CRE calculations likely utilize more accurate radiative and atomic models than those contained within the radiation-hydrodynamics code. It must be emphasized, however, that in the absence of reliable experimental data, the accuracy of both calculations is open to question. Nevertheless, our calculations indicate that it is not unlikely that the LASNEX simulations may be overestimating the radiation losses from the Al layer by a factor of a few. This, coupled with the fact that the peak temperature predicted by the radiation-hydrodynamics simulations depends sensitively on the opacities used, suggests the "inconsistency" between the measured Li beam properties and measured K_α spectra may, at least in part, be due to inaccuracies in the LASNEX radiation modeling. Additional calculations are currently being performed to further investigate this issue.

Acknowledgment

Support for this work has been provided by the U.S. Department of Energy through Sandia National Laboratories.

References

Bailey, J.E., Carlson, A.L., Chandler, G., Derzon, M.S., Dukart, R.J., Hammel, B.A., Johnson, D.J., Lockner, T.R., Maenchen, J., McGuire, E.J., Mehlhorn, T.A., Nelson, W.E., Ruggles, L.E., Stygar, W.A., and Wenger, D.F., *Lasers & Particle Beams* **8**, 555 (1990).

Bailey, J.E., private communication (1993).

Bailey, J.E., et al., presented at the 6th International Workshop on Atomic Physics for Ion-Driven Fusion, Santa Fe, NM (1993).

Boiko, V.A., Faenov, A.Ya., and Pikuz, A., *J. Quant. Spectrosc. Radiat. Transfer* **19**, 11 (1978).

Chen, M., and Iglesias, C., private communication (1993).

Cowan, R.D., "The Theory of Atomic Structure and Spectra," University of California Press, Berkeley (1981).

Dukart, R.J., private communication (1993).

Fano, U., *Phys. Rev.* **124**, 1866 (1961).

MacFarlane, J.J., and Wang, P., *Phys. Fluids B* **3**, 3494 (1991).

MacFarlane, J.J., and Wang, P., "Theoretical Spectral Diagnostic Analysis in Support of PBFA-II Beam-Plasma Interaction Experiments," University of Wisconsin Fusion Technology Institute Report UWFDM-913 (1993).

MacFarlane, J.J., Wang, P., Bailey, J., Mehlhorn, T.A., Dukart, R.J., and Mancini, R.C., *Phys. Rev. E* **47**, 2748 (1993).

Mihalas, D., Stellar Atmospheres, Second Edition, (Freeman, New York, 1978).

Perry, T.S., Davidson, S.J., Serduke, F.J.D., Bach, D.R., Smith, C.C., Foster, J.M., Doyas, R.J., Ward, R.A., Iglesias, C.A., Rogers, F.J., Abdallah, J., Stewart, R.E., Kilkenny, J.D. and Lee, R.W., *Phys. Rev. Lett.* **67**, 3784 (1991).

Wang, P., MacFarlane, J.J. and Moses, G.A., *Phys. Rev. E* **48**, 3934 (1993).

Plasma Diagnostics Using K_α Satellite Emission Spectroscopy in Light Ion Beam Fusion Experiments

J. J. MacFarlane and P. Wang

Fusion Technology Institute
University of Wisconsin
Madison, WI 53706

J. E. Bailey, T. A. Mehlhorn, and R. J. Dukart

Sandia National Laboratories
Albuquerque, NM 87185

January 1994

UWFDM-941

Submitted for publication to Lasers and Particle Beams as part of the 6th International Workshop on Atomic Physics for Ion Driven Fusion.

Effects of Multiple Ionization on the K_α Spectrum of Aluminum in Intense Lithium Beam Experiments

P. Wang, J. J. MacFarlane, and G. A. Moses

Fusion Technology Institute
University of Wisconsin-Madison
1500 Johnson Drive
Madison, WI 53706

January 1994

UWFDM-938

Submitted for publication to Lasers and Particle Beams as part of the 6th International Workshop on Atomic Physics for Ion Driven Fusion, 8–12 November 1993, Santa Fe NM